Resource

Cell Reports

Deformation Microscopy for Dynamic Intracellular and Intranuclear Mapping of Mechanics with High Spatiotemporal Resolution

Graphical Abstract

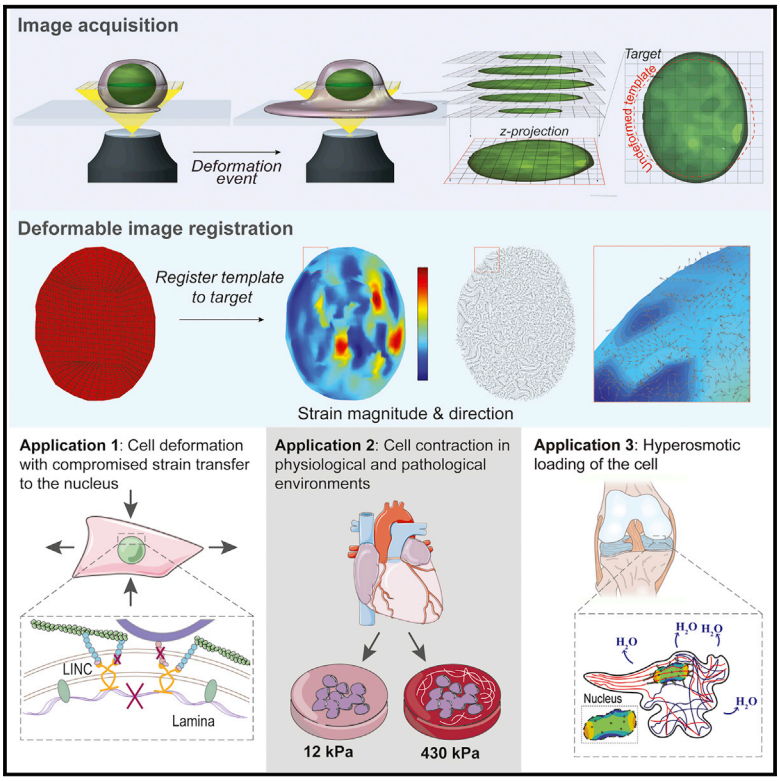

Highlights

- Deformation microscopy is developed by combining imaging and advanced mechanics
- Modulation of nuclear LINC proteins or lamin A/C reveals altered intranuclear strain
- Abnormal mechanical environments cause abnormal strain in high-density chromatin
- Hyperosmotic conditions lead to nuclear strain asymmetry mediated by the cytoskeleton

Authors

Soham Ghosh, Benjamin Seelbinder, Jonathan T. Henderson, Ryan D. Watts, Adrienne K. Scott, Alexander I. Veress, Corey P. Neu

Correspondence

cpneu@colorado.edu

In Brief

Ghosh et al. show that deformation microscopy, a technique based on image analysis and mechanics, reveals deformation dynamics and structural heterogeneity changes for several applications and at multiple scales, including tissues, cells, and nuclei. They reveal how the disruption of nuclear proteins and pathological conditions abrogate mechanical strain in the nuclear interior.

Ghosh et al., 2019, Cell Reports *27*, 1607–1620
April 30, 2019
https://doi.org/10.1016/j.celrep.2019.04.009

CellPress

Cell Reports
Resource

Deformation Microscopy for Dynamic Intracellular and Intranuclear Mapping of Mechanics with High Spatiotemporal Resolution

Soham Ghosh,[1,4] Benjamin Seelbinder,[1,4] Jonathan T. Henderson,[2] Ryan D. Watts,[2] Adrienne K. Scott,[1] Alexander I. Veress,[3] and Corey P. Neu[1,2,5,*]
[1]Department of Mechanical Engineering, University of Colorado Boulder, Boulder, CO, USA
[2]Weldon School of Biomedical Engineering, Purdue University, West Lafayette, IN, USA
[3]Department of Mechanical Engineering, University of Washington, Seattle, WA, USA
[4]These authors contributed equally
[5]Lead Contact
*Correspondence: cpneu@colorado.edu
https://doi.org/10.1016/j.celrep.2019.04.009

SUMMARY

Structural heterogeneity is a hallmark of living cells that drives local mechanical properties and dynamic cellular responses. However, the robust quantification of intracellular mechanics is lacking from conventional methods. Here, we describe the development of deformation microscopy, which leverages conventional imaging and an automated hyperelastic warping algorithm to investigate strain history, deformation dynamics, and changes in structural heterogeneity within the interior of cells and cell nuclei. Using deformation microscopy, we found that partial or complete disruption of LINC complexes in cardiomyocytes *in vitro* and lamin A/C deficiency in myocytes *in vivo* abrogate dominant tensile loading in the nuclear interior. We also found that cells cultured on stiff substrates or in hyperosmotic conditions displayed abnormal strain burden and asymmetries at interchromatin regions, which are associated with active transcription. Deformation microscopy represents a foundational approach toward intracellular elastography, with the potential utility to provide mechanistic and quantitative insights in diverse mechanobiological applications.

INTRODUCTION

Mechanobiology is an emerging field that describes how mechanical forces modulate the structure and function of biological tissues and that affects the development, homeostasis, disease, and engineering of biological systems (Iskratsch et al., 2014). Physical stimuli of cells, including forces and stretching applied to the cell membrane, transfer to the cell and nuclear interior and result in microscale deformations that are critical structural and biophysical parameters in mechanobiology. The deformation of different cellular components can trigger unique biochemical pathways and mechanotransduction cascades and regulate diverse processes, including adhesion and differentiation (Wang et al., 2009).

In recent years, studies have focused on how mechanical cues are transmitted to the nucleus to influence gene regulation and chromatin organization (Guilluy et al., 2014; Denais et al., 2016; Raab et al., 2016; Tajik et al., 2016). The cell nucleus is known to contain, maintain, and interpret the genomic information that forms the basis for every individual. The nucleus is also subject to significant deformation, especially in mechanically active tissues such as the heart, skeletal muscle, and cartilage. Force is transmitted to the nucleus through direct physical connections to the cytoskeleton via the LINC (linker of nucleoskeleton and cytoskeleton) complexes comprising Sad1p, UNC-84 (SUN), and nuclear envelope spectrin repeat (nesprin) proteins (Crisp et al., 2006; Isermann and Lammerding, 2013; Alam et al., 2016). SUNs bind the nuclear lamina, stretch through the inner nuclear membrane, and connect to nesprins in the perinuclear space via highly conserved Klarsicht, ANC-1, Syne Homology (KASH) domains (Alam et al., 2016). Nesprins, in turn, span through the outer nuclear membrane and connect to different parts of the cytoskeleton, with nesprin-1 and nesprin-2 binding to actin, nesprin-3 to intermediary filaments, and nesprin-4 to microtubules (Stroud et al., 2014). Force transmission to the nucleus is also affected by the nuclear lamina, a fibrillar structure inside the nuclear membrane comprising lamin A/C and lamin B. The nuclear lamina is thought to be associated with chromatin through nuclear envelope transmembrane proteins (NETs) (Wilkie et al., 2011; Solovei et al., 2013; Zuleger et al., 2013). Through these intertwined connections, mechanical cues at the tissue level can be transmitted to and are thought to be processed within the nucleus to influence gene expression (Driscoll et al., 2015), cell differentiation (Banerjee et al., 2014), cancer cell migration (Denais et al., 2016), nucleoskeleton rearrangement (Guilluy et al., 2014; Swift and Discher, 2014), and chromatin organization (Iyer et al., 2012; Heo et al., 2015; Seelbinder et al., 2018).

The detrimental effects of disrupting the LINC complex and the nuclear lamina motivate a thorough investigation of nuclear mechanotransduction. Mutations in the LINC complex and

nuclear envelope proteins are linked to developmental disorders, particularly in mechanically active tissues such as cardiac and skeletal muscle (Taranum et al., 2012; Banerjee et al., 2014). There are many nuclear lamina-associated diseases, broadly termed laminopathies, that are characterized by different mutations in lamin A/C proteins, eventually rendering a mechanically weak nuclear lamina. One of the most severe manifestations is observed in Hutchinson-Gilford progeria syndrome patients in whom, due to a point mutation, a defective form of lamin A/C is expressed that cannot integrate with the nuclear lamina (Taimen et al., 2009). Consequently, patients display symptoms of accelerated aging and rarely reach the age of 20 due to cardiovascular deficiencies. It is worth mentioning that softer, mechanically inactive tissues such as the brain are not affected in progeria patients, further highlighting the link between tissue mechanics and nuclear mechanics. Thus, nuclear mechanics seems to play an important role in tissue development and function. Despite the growing interest in and importance of nuclear mechanobiology, conventional methods to quantify cell and nuclear deformation lack the capability to generate high-resolution spatial strain maps. These spatial strain maps are needed to elucidate how nuclear strain influences the regulation patterns of gene expression with respect to genomic organization and activation.

Numerous important methods have been described to measure cell mechanics, each with their own strengths and limitations (Wu et al., 2018). For the nucleus, the most commonly used techniques are based on the quantification of simple morphological changes such as aspect ratio, volume, or a characteristic dimension (Knight et al., 2002; Gilchrist et al., 2007). This type of analysis only considers geometric changes of the nuclear periphery and does not provide any intranuclear spatial information. Edge detection, fluorescence anisotropy (Talwar et al., 2013), and texture correlation (Gilchrist et al., 2007; Henderson et al., 2013) techniques provide only low-resolution spatial information and are typically limited to two dimensions. Moreover, they are overly sensitive to noise and often require sharp spatial features that are typically not well defined in image data. In contrast, deformable image registration offers a more rigorous approach as it can quantify intranuclear deformation at high spatial resolution, as demonstrated in intact tissue systems (Henderson et al., 2013). With this technique, local differences in image intensities are used to match a discretized template image (undeformed) with a target (deformed) image to obtain deformation maps (Brock et al., 2005). However, there are several tunable parameters in the underlying algorithm that need to be defined, and numerous technical challenges exist for achieving a reliable deformation map before exploring potential new biological insights (Veress et al., 2004). Consequently, defining a suitable method to map deformation or a correct set of parameters to obtain an optimal deformation map in a manageable time frame is challenging and largely lacking. In our previous work, we created the basic framework for such deformation quantification (Henderson et al., 2013), which requires an experienced user to generate the deformation map by manually changing the tunable algorithm parameters, and consequently the technique also demands significant computational time. In the present study, we validate and demonstrate the application of an improved technique, deformation microscopy, which automates the analysis and can be used by any inexperienced user to quantify precise, high-resolution, reliable spatial patterns of intracellular displacements and strain.

Deformation microscopy is versatile and can be applied over multiple biological length scales. To rigorously validate this technique, we applied a known, simulated deformation map on microscopic images. We used this baseline known deformation map to reproduce the calculated deformation map obtained by the deformation microscopy technique. After validation, we demonstrated the ability to generate strain maps of tissues, cells, and nuclei under deformation *in vitro* and *in vivo*. Because of the increasing importance of understanding nuclear mechanobiology, we focused our experiments on investigating the spatiotemporal mechanics of nuclei in several physiological and pathological conditions. We showed that strain transfer to the nucleus was compromised after disruption of the LINC complex during cardiomyocyte contractions *in vitro* and in a lamin A/C-deficient mouse model *in vivo*. Furthermore, we demonstrated a difference in nuclear strain between cardiomyocytes cultured in physiological (soft) and pathologic (stiff) environments and showed that strain was concentrated to high-density chromatin regions during cell contraction. We additionally showed that deformation microscopy can be combined with established methods such as traction force microscopy to correlate intracellular and intranuclear strains. Using this approach, we showed how the cytoskeleton architecture contributes to asymmetric strain propagation during hyperosmotic loading in passaged chondrocytes. Therefore, through multiple biological applications, we demonstrate how high-resolution intranuclear strain can be used to gain a deeper understanding of the role of nuclear mechanics in physiological and pathological processes.

RESULTS

Deformation Microscopy Is a Versatile Tool to Quantify Spatial Strains across Different Length Scales

Deformation microscopy was developed to quantitatively map the strain distributions within the cellular and nuclear interiors. High-resolution displacement and strain maps are obtained from the microscopy images acquired before and after deformation events (Figures 1A and S1; Methods S1 and S2; see STAR Methods for details). Small image features are tracked in image sets by image registration, which allows for the measurement of deformation, including strain magnitude and direction (e.g., high-resolution principal strains in Figure 1A, inset red box), with the measurement sensitivity limited only by the image quality. The technique was validated by analyzing known (simulated) deformations using a nucleus with defined structural and material properties. Calculated deformation maps were then compared to the simulated deformations, which served as gold standard values (Figures 1B, 2, S2, and S3; Methods S3). Over a wide range of properties for defined intranuclear regions, we were able to match simulated and calculated deformations, validating the ability to obtain reliable strain maps. By processing displacements to remove the effects of rigid body motion (e.g., rotations, translations), different modes of deformation and resulting strain measures can be attained, including hydrostatic, deviatoric,

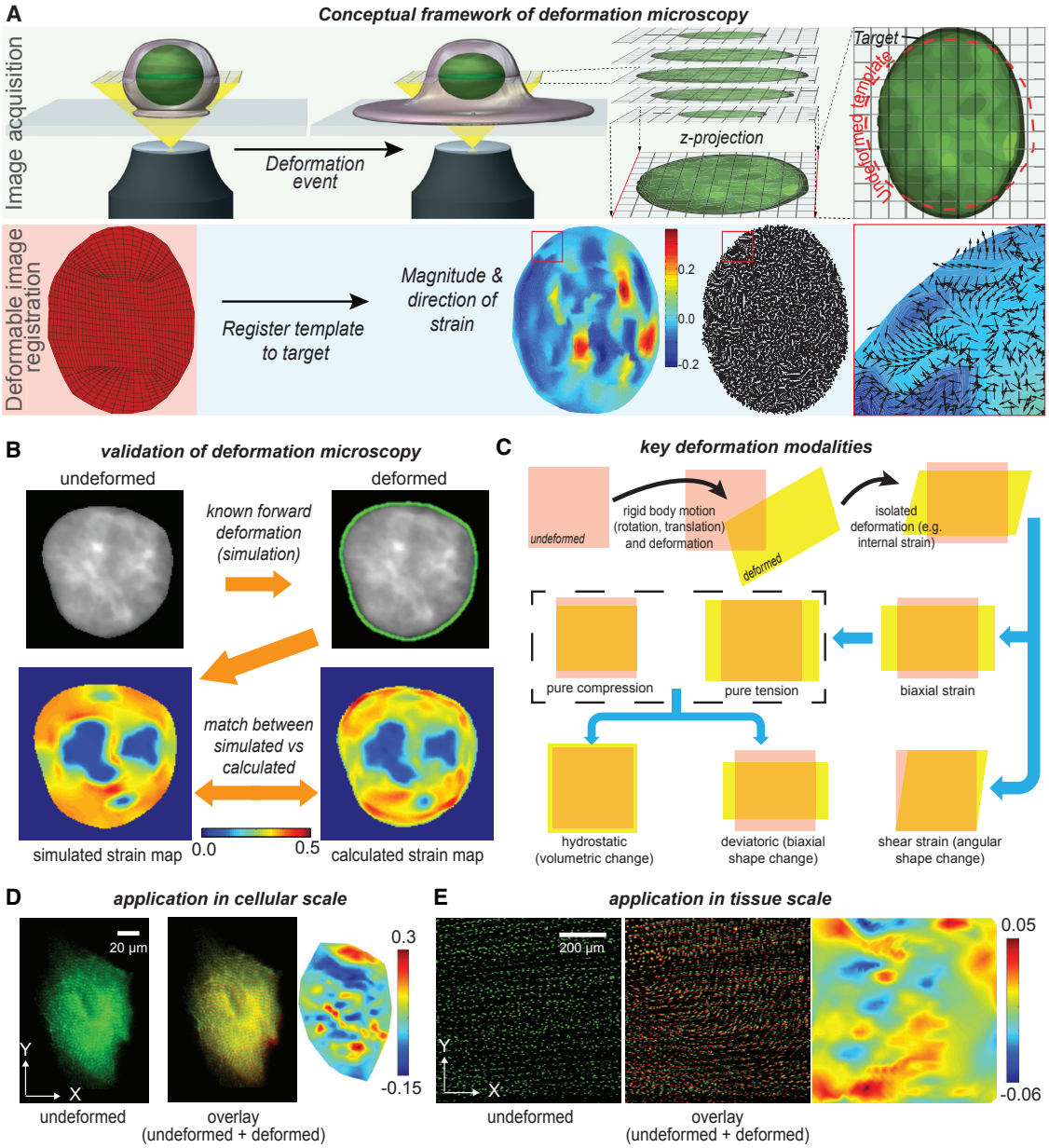

Figure 1. Validation of Strain Measurements Using Deformation Microscopy, and Use of Method on Multiple Biological (Cell and Tissue) Length Scales

(A) Illustrated deformation microscopy workflow for generating strain maps, using the cell nucleus as an example. Nuclear z stacks in undeformed (template) and deformed (target) states are acquired using confocal microscopy. z projections are then generated to carry out the deformation quantification in a two-dimensional framework. After a mesh for the template nucleus is generated, a mathematical model uses the iterative hyperelastic warping algorithm to quantify intranuclear strain by registering the undeformed image to the deformed image. The result is a high-resolution spatial deformation map. Shown here is a deformation surface map and deformation vector direction map of the interior strain. The overlap of deformation value (magnitude) and direction is shown in the magnified image panel for the red inset area.

(B) For validation, the finite element modeling software ANSYS was used to apply a known (simulated) deformation on the nucleus image. The known deformation map obtained by forward simulation was compared with the deformation map obtained by deformation microscopy.

(C) The physical interpretation of the key strain measures such as tension, compression, hydrostatic, shear, and deviatoric strains are detailed.

(D) Embryonic cardiomyocytes were transduced with a vector expression α-Actinin-mRuby2, and sarcomeres were imaged during spontaneous contractions. Undeformed (green) and overlay (undeformed: green + deformed: red) image stacks are shown. Image stacks were used to calculate the strain maps via deformation microscopy, and a map with strain in the y direction is shown.

(E) Skeletal muscle was stained with NucBlue live DNA stain and contracted through electrostimulation *in vivo*. Stained nuclei were used to define texture and fiducial marks in the muscle, thus demonstrating the feasability of the technique on the tissue scale. Undeformed (green) and overlay (undeformed: green + deformed: red) image stacks are shown. The strain map shows hydrostatic strain.

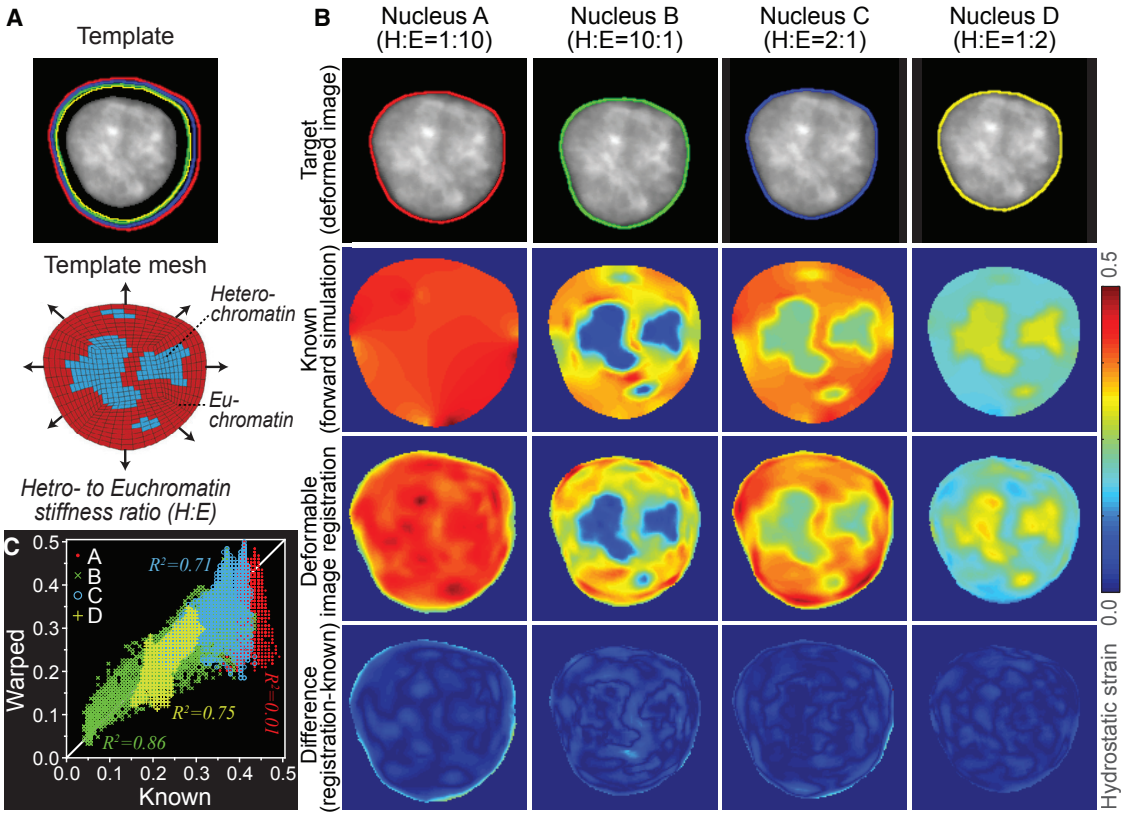

Figure 2. Validation of the Deformation Microscopy Technique by Matching Known (Forward Simulation) and Calculated Strain Maps

(A) The template nucleus was subjected to uniform outward normal force along the nucleus perimeter. The intranuclear region was meshed and segmented into a low-density euchromatin region (red area) and a high-density heterochromatin area (blue area). Green, yellow, red, and blue outlines show the deformed target nucleus perimeter for different heterochromatin-to-euchromatin (H:E) stiffness ratios.

(B) The top row shows the deformed target images. Hydrostatic strain maps are shown using forward finite element simulation (second row) or deformable image registration (third row). The bottom row shows the difference between forward simulation and deformable image registration. Note that the difference was near zero throughout the nuclear domain.

(C) Quantitative comparison of hydrostatic strain maps generated by deformable image registration compared to known strains from forward simulations. The best match is obtained for the physiologically relevant H:E stiffness ratio of 2:1 (R^2 = 0.86).

shear, tensile, and compressive strains (Figure 1C; Methods S4), which are frequently used in the following results. We further demonstrated the utilization of deformation microscopy across different biological length scales and applications. We quantified the deformation maps of a single beating cardiomyocyte *in vitro* (Figure 1D) and in skeletal muscle tissue *in vivo* (Figure 1E) using image information before and after contraction, respectively.

Disruption of LINC Complexes in Cardiomyocytes *In Vitro* and Lamin A/C Deficiency in Myocytes *In Vivo* Revealed Altered Nuclear Strain Transfer

The chromatin architecture inside the nucleus is connected to the cytoskeleton through LINC complexes and the nuclear lamina. Mutations in the LINC complex and nuclear lamina are linked to developmental disorders and pathological conditions, particularly in mechanically active tissues such as cardiac and skeletal muscle (Taranum et al., 2012; Isermann and Lammerding, 2013; Banerjee et al., 2014), suggesting that nuclear strains play an important role in tissue development and function. Using our deformation microscopy methods, we aimed to quantify nuclear strains in two different models in which nuclear strain transfer was hypothesized to be compromised: (1) during cyclic contractions in embryonic cardiomyocytes after knock down of nesprin-3 or overall disruption of LINC complexes via the expression of a negative dominant KASH construct *in vitro* and (2) in the myocytes of lamin A/C-deficient mice during skeletal muscle stimulation *in vivo*.

Cardiomyocytes were derived from embryonic mice (embryonic day [E] 18.5) that harbored an EGFP-tag at the H2b histone (*H2b-EGFP*) to visualize chromatin during live cell imaging (see Method Details). Embryonic cardiomyocytes were plated on soft (12 kPa) polydimethylsiloxane (PDMS) to mimic the stiffness of adult cardiac environments (Engler et al., 2008), and cardiomyocytes developed spontaneous contractions within 1 day of culture. We hypothesized that the disruption of LINC complexes should significantly alter intranuclear strain intensities during cardiomyocyte contractions. To test this hypothesis, cardiomyocytes were transduced with vectors to knock down nesprin-3 (shSyne3) or express a dominant-negative KASH construct (TmKash3) that displaces native nesprins via the KASH domain

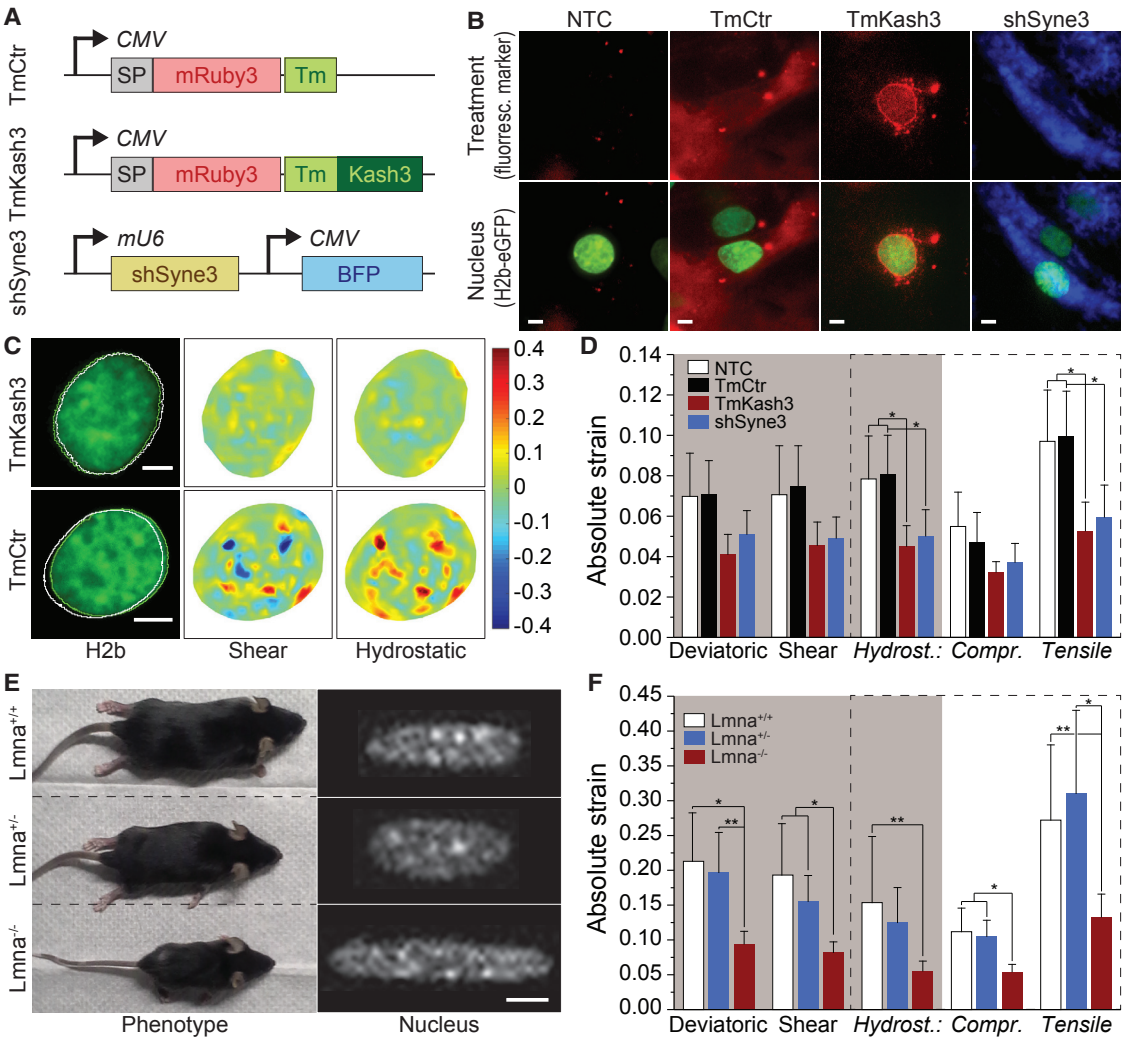

Figure 3. Partial or Complete Disruption of LINC Complexes in Cardiomyocytes *In Vitro* and Lamin A/C Deficiency in Myocytes *In Vivo* Revealed Altered Nuclear Strain Transfer

(A) Schematic of vectors for LINC complex disruption; SP, signal peptide; Tm, transmembrane domain.

(B) H2b-EGFP expressing cardiomyocytes after transduction with different vectors to disrupt LINC complexes. Red fluorescence indicates the successful integration of the dominant-negative KASH vector (TmKash3) into the nuclear membrane; NTC, non-transduced control.

(C) Nuclear strain maps generated via deformation microscopy for a nucleus transduced with the decoupling vector TmKash3 or the control vector TmCtr. Intranuclear strains were reduced after decoupling; white lines, nuclear boundary at peak contraction.

(D) Differential strain analysis of decoupled and control cardiomyocyte nuclei revealed lower hydrostatic strain, particularly tensile hydrostatic strain, in decoupled (TmKash3) and nesprin-3 knockdown (KD) (shSyne3) nuclei compared to transduced (TmCtr) or non-transduced or control cells; n = 6, error = SD, *$p < 0.05$.

(E) Overall physiological and nuclear phenotypes of hemizygote and homozygote ($Lmna^{-/-}$) lamin A/C mice compared to wild-type littermates.

(F) *In vivo*, for the same tissue strain (pre-calibrated), nuclear strain in skeletal muscle was significantly lower in $Lmna^{-/-}$ mice compared to wild-type ($Lmna^{+/+}$) and hemizygote ($Lmna^{+/-}$) carriers; n = 9, error = SD, *$p < 0.05$, **$p < 0.01$, all scales, 5 μm.

but lacks cytoskeleton binding domains (Figures 3A and S4). A control construct (TmCtr) was designed that was identical to TmKash3 but lacked the KASH domain to compete with nesprins for SUN connections. Successful nuclear membrane integration of TmKash3 or TmCtr was tracked via a N-terminal fluorescence protein (mRuby3) and shSyne3-expressing cells were identified via the expression of a blue fluorescent protein (BFP; Figure 3B). TmKash3 formed a distinct ring around the nuclear border and replaced nesprin-1, indicative of successful LINC complex integration, while TmCtr did not, and gene expression analysis confirmed the successful knock down of nesprin-3 in shSyne3-transduced cardiomyocytes (Figures 3B and S4). Nesprins span through the outer nuclear membrane and connect to different parts of the cytoskeleton. In cardiomyocytes, intermediary filaments are mainly represented by desmin, which encases all sarcomeres in a honeycomb-like fashion and laterally integrates with costamers, which in turn connect to the underlying extracellular matrix (Sarantitis et al., 2012). Desmin therefore provides an important structure to transfer strain from sarcomeres to the tissue and vice versa. Nesprin-3 was specifically

targeted here, as it connects to desmin and is largely understudied. Both the knock down of nesprin-3 and the overall LINC disruption via TmKash3 expression led to a reduction of intranuclear strains, particularly for hydrostatic strain, compared to cells transduced with the control vector TmCtr or non-transduced control cells (NTC; Figures 3C and 3D). Since hydrostatic strains represent a change in volume, we could further separate this strain measure into tensile (positive) and compressive (negative) hydrostatic strains. This analysis showed that mostly tensile hydrostatic strains were reduced after LINC disruption, while only a small change was observed for compressive hydrostatic strains, as would be expected from cell contraction that imparts significant tensile forces throughout the cell. In addition, there was only a small difference in nuclear strain reduction between the disruption of all nesprins or only nesprin-3, highlighting the importance of nesprin-3 for nuclear strain transfer in cardiomyocytes. It should be noted, however, that the expression of shSyne3 also partially reduced the mRNA of nesprin-1 and -2 (Figure S4).

Next, we were interested in whether disruption of the nuclear lamina, which provides mechanical resilience to the nucleus, affects tissue-to-nucleus strain transfer *in vivo*. For this analysis, we imaged nuclei during hindlimb muscle stimulation in a lamin A/C-deficient murine model. The mice harbored a mutated *Lmna* gene that leads to the expression of a truncated lamin A/C protein that is unable to form a meshwork, hence leading to a mechanically compromised nuclear lamina. Similar to laminopathy in humans, homozygote lamin A/C-deficient mice showed extensive developmental retardation, causing death before reaching full maturity (~8 weeks), as well as changes in nuclear morphology (Figure 3E). Experiments *in vitro* found that there is a higher strain transfer to lamin A/C-deficient nuclei and conclude that nuclei are softer due to the compromised nuclear envelope (Zwerger et al., 2017). In contrast, atomic force microscopy (AFM) studies on single-cell nuclei observed stiffer mechanical properties of nuclei in lamin A/C-deficient cells (Lanzicher et al., 2015). Therefore, the mechanical role of lamin A/C and the resulting effect on nuclear strain transfer are still debated and have not been studied *in vivo* so far. We found that for the same amount of tissue deformation, all measures of nuclear strain decreased in homozygote lamin A/C-deficient mice ($Lmna^{-/-}$) by 40%–50% compared to $Lmna^{+/+}$ wild-type mice (Figure 3F). Similar to our observations in cardiomyocytes after the LINC complex disruption, strain reduction was the most prominent for tensile hydrostatic strains, but not for compressive strains. Hemizygote mice ($Lmna^{+/-}$) showed only a minor decline in nuclear strains. These mice also show only minor developmental retardation and are viable and fertile, highlighting a link between nuclear strain and development. These results showed that the disruption of nucleoskeleton components, which are associated with developmental perturbations, lead to a decline in nuclear strain transfer.

Cardiomyocyte Nuclear Strain Concentrates to Low-Density Chromatin Regions during Contraction and Is Altered When Cultured on Physiological or Stiff Substrates

Experiments *in vitro* have shown that cardiomyocytes modulate their beating behavior based on the stiffness of their environment, with optimal beating properties being observed on substrates that resemble the healthy native heart stiffness (10–20 kPa), whereas contractile forces decline on stiffer substrates (Engler et al., 2008). Various conditions lead to the stiffening of the cardiac environment, including hypertrophy, cardiac fibrosis, and the formation of fibrotic scar tissue after cardiac infarction (Fan et al., 2012; Dingal et al., 2015). Since abrogated nuclear strain transfer has been associated with developmental disruption in cardiovascular tissue, the decline in contraction, and therefore nuclear deformation, may also contribute to the degeneration of fibrotic cardiac tissues. However, no investigation of cardiac intranuclear strains and their change with substrate stiffness as seen in disease has been conducted previously. Here, we aimed to use deformation microscopy to generate high-resolution intranuclear strain maps of contracting cardiomyocytes on stiff and soft substrates. Furthermore, chromatin is organized within nuclei (Joffe et al., 2010; Pombo and Dillon, 2015) and on the simplest level can be separated into different states of compaction with dense heterochromatin, typically containing silenced genes, and sparsely packed euchromatin containing actively transcribed genes. The intranuclear strain maps were therefore additionally compared to chromatin compaction states to understand the effect of fibrotic environments and strain transfer on chromatin organization.

For the present study, *H2b-EGFP*-harboring cardiomyocytes were plated on either soft (~12 kPa) or stiff (~434 kPa) PDMS substrates to mimic native and pathologically stiffened environments. At day 4 of culture, image series (~6.4 frames per second [fps]) of nuclei during contractions were acquired, and one contraction cycle was picked for each nucleus to perform an in-depth intranuclear strain analysis (Figures 4A, 4B, and 5). Fluorescence from H2b, a histone protein present in all nucleosome complexes that scaffold DNA into chromatin, was used as a marker for local chromatin compaction to spatially correlate nuclear strain with chromatin density. Chromatin intensity values were rescaled to [−1 +1] to compare strain data from different nuclei. Image frames in the post-diastolic resting states were selected, as undeformed reference images (template) and t_1–t_4 represent the deformed states during the contraction cycle. Cardiomyocytes plated on soft substrates displayed high tensile and compressive hydrostatic nuclear strains that peaked at ~t_2 and gradually decreased again (Figures 4A and 5; Video S1). On stiff substrates, cardiomyocyte contractions were shortened, resulting in fewer sequential images during each contraction cycle, and nuclear strains were almost one order of magnitude lower compared to the soft substrates. Changes in nuclear strain during one contraction cycle varied along different chromatin compaction states for cells on both substrates. Absolute hydrostatic strains increased mostly for low-density chromatin, becoming less significant toward medium density and showed almost no changes for dense chromatin (Figure 4B). In contrast, changes in absolute shear and deviatoric strains were most prominent for medium-density chromatin. This difference in strain prominence across different chromatin densities was further confirmed for n = 5 nuclei during peak contraction (Figure 4C).

Strain trends were similar between cells on soft or stiff substrates. However, since changes in nuclear strain differed along

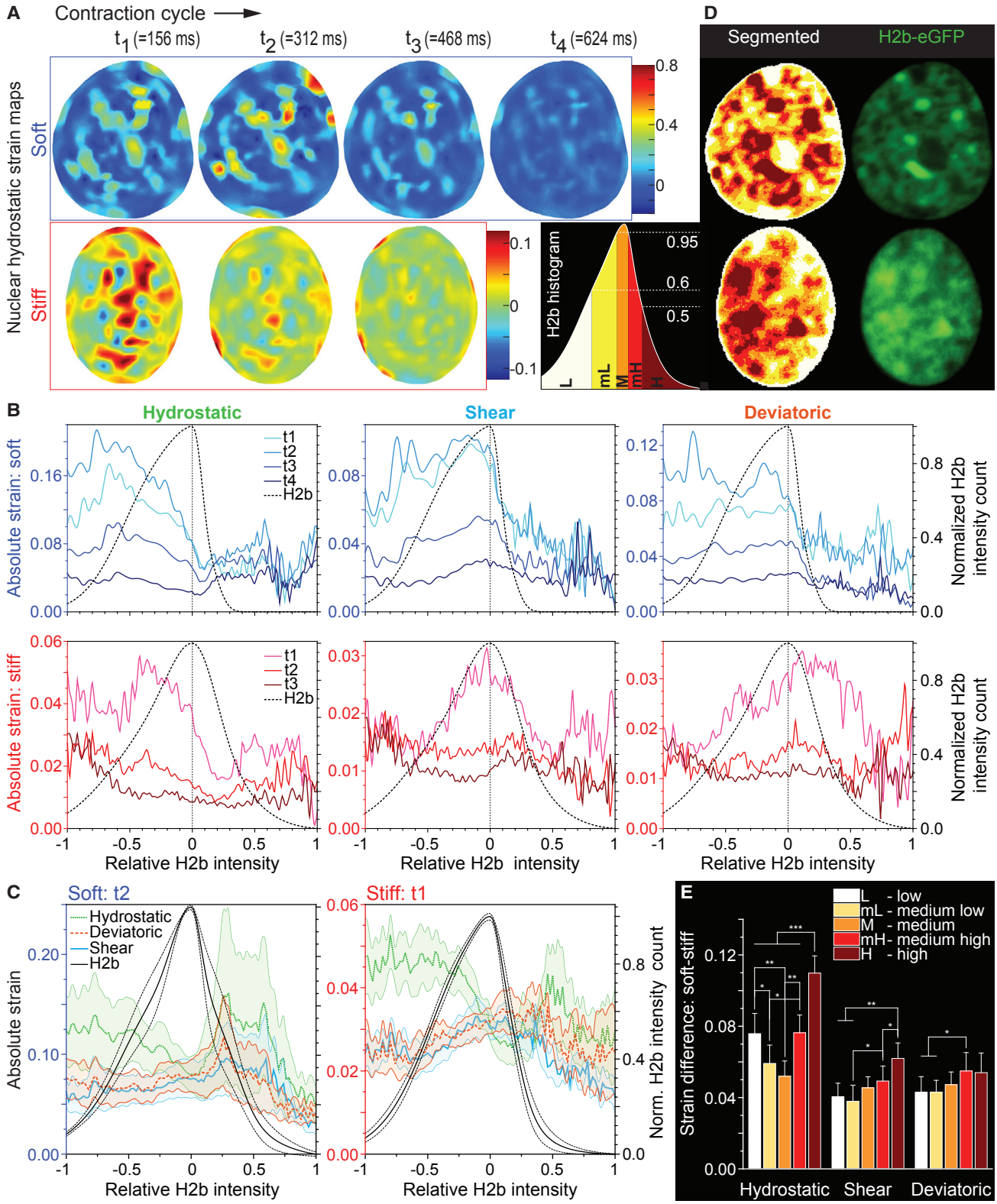

(legend on next page)

chromatin compaction during contraction, we were further interested in whether the decline of nuclear strain on stiff substrates also varied for different chromatin densities. Chromatin intensity histograms were binned into 5 areas with roughly equal numbers of data points for each density region: [0; 0.6] for low, [0.6; 0.95] for medium low, [0.95; 0.95] for medium, [0.95; 0.5] for medium high, and [0.5; 0] for high chromatin density (Figure 4D). The highest discrepancies in nuclear strain between soft and stiff substrates were observed for hydrostatic strains, with medium-density chromatin showing the lowest level of change (Figures 4E and S4D). High-density chromatin showed the largest difference, being twice as high compared to medium-density chromatin (11.0% versus 5.2%), even though it was the least affected during the contraction cycles. Chromatin with low density also experienced a higher decline in strain 1.5 times that of medium-density chromatin (7.6% versus 5.2%). Deviatoric and shear strains showed less distinct discrepancies in strain decline between substrates; however, the most prominent changes were observed for high-density chromatin again.

With both high tensile and compressive strains, this model was further well suited to demonstrate that bulk strain analysis methods underestimate actual strain values because they allow local intranuclear strains to cancel one another out by only considering deformation at the nuclear boundary. To support this idea, we compared averaged absolute hydrostatic strains generated from our deformation microscopy analysis (avg(abs(ε_{hyd}))) against bulk strains calculated from the average change in the minor and major axes (abs(ε_{bulk})), as typically used to estimate nuclear strains (Figure S4C) (Driscoll et al., 2015). To show that the underestimations in bulk strain are a result of neglecting intranuclear strains, we calculated another value in which hydrostatic strains were first averaged and then made absolute (abs(avg(ε_{hyd}))) to allow for the same effect. As anticipated, averaged absolute local strains were twice as high compared to bulk strains for both soft and stiff (soft: 11.1% versus 4.6% and stiff: 3.2% versus 1.8%), while hydrostatic strains that were first averaged showed almost identical values. Note that local extrema can be up to 10 times higher compared to averaged hydrostatic strains or 20 times higher compared to bulk strain estimates, respectively. These results show that low-density chromatin experienced higher levels of change and higher overall hydrostatic strain during cardiomyocyte contractions, while high-density chromatin showed a more prominent decline in strain for cells plated on stiff substrates compared to soft. These data also demonstrate that spatial nuclear strain maps obtained from our deformation microscopy method provide not only a better estimate of nuclear bulk strains but also additional detail and insight into nuclear mechanics through a combined analysis with other spatial information.

Asymmetric Nuclear Strains during Hyperosmotic Loading of Chondrocytes Relates to Cytoskeleton Organization

We wanted to further validate the quantification of nuclear strains via deformation microscopy in a physiological relevant and well-defined biological system. Cartilage goes through cycles of hyperosmotic and hypoosmotic shock during motion due to its poroelastic nature, with large variations in hydration and pressurization levels. Changes in osmotic pressures mediate intracellular water transport, which causes cell and nuclear deformation, both of which have been linked to altered gene expression in chondrocytes (Peffers et al., 2010). We imaged the progressive deformation of passage 4 (P4) chondrocyte nuclei for 12 min after hyperosmotic loading (Figure 6A; Video S2). Using conventional measurements, we observed a decline in nuclear area and compressive nuclear engineering strains, as determined by the length of the nuclear major axis, with temporal progressions of hyperosmotic loading (Figure S5) as expected due to the extrusion of water. This trend in nuclear strains could be recapitulated using deformation microscopy, which further showed that hydrostatic strains were most affected and became more compressive (negative) over time (Figure 6C). Next, we used traction force microscopy (Martiel et al., 2015) to calculate substrate stress relaxation during hyperosmotic loading from the displacement of fluorescent beads embedded into the substrate using the undeformed state after trypsin-mediated cell release as reference (Figure 6A). Substrate traction forces were highest near the cell apices and declined over time due to cell shrinkage, as reported previously (Califano and Reinhart-King, 2010). Substrate stress relaxation maps could then be generated as the difference in traction force using the start of the treatment (0 min) as a reference (Figure 6B). Analysis of nuclear strains with stress relaxation over time or over the endpoint (11 min) in chondrocytes revealed that volume change-related hydrostatic strains were significantly correlated with both nuclear strain and stress relaxation (R^2 = 0.99; Figure 6D). In contrast, shape

Figure 4. Intranuclear Strain in Cardiomyocytes Concentrates to Low-Density Chromatin Regions during the Contraction but Reveals the Highest Strain Discrepancy for High-Density Chromatin between Physiological or Pathological Mechanical Environments

Cardiomyocytes expressing H2b-EGFP were plated on soft (~12 kPa, physiological) or stiff (~434 kPa, pathological) PDMS substrates, and image stacks of nuclear deformation during contraction were recorded.

(A) Hydrostatic strain maps for different time steps during contraction (t_1, t_2, t_3, t_4) were generated via deformation microscopy using fluorescence image stacks with diastolic resting state as the undeformed template.

(B) Nuclear strains were analyzed in relation to the chromatin density as inferred by H2b intensity. To allow for comparison, H2b intensity was normalized to [−1, 1], with the peak of each distribution set to 0. Lines present different time steps during one contraction cycle, as reported in (A). Low-density chromatin showed higher changes in the strain during contraction compared to high-density chromatin.

(C) Absolute nuclear strains at peak contraction over chromatin density for n = 5 cells plated on either stiff or soft substrates; areas = SEMs.

(D) Left: representative segmentation of a chromatin intensity histogram into low- (L), medium low- (mL), medium- (m), medium high- (mH), and high- (H) density chromatin, with each area having approximately equal data points (pixels analyzed). Right: resulting segmentation map and corresponding nuclear H2b-EGFP intensity map from the nuclei shown in (A).

(E) The difference in absolute nuclear strain between cardiomyocytes plated on soft or stiff substrates for each chromatin density segment. High-density chromatin revealed the most prominent differences for hydrostatic strain; n = 5, error = SD, *p < 0.05, **p < 0.01, ***p < 0.001.

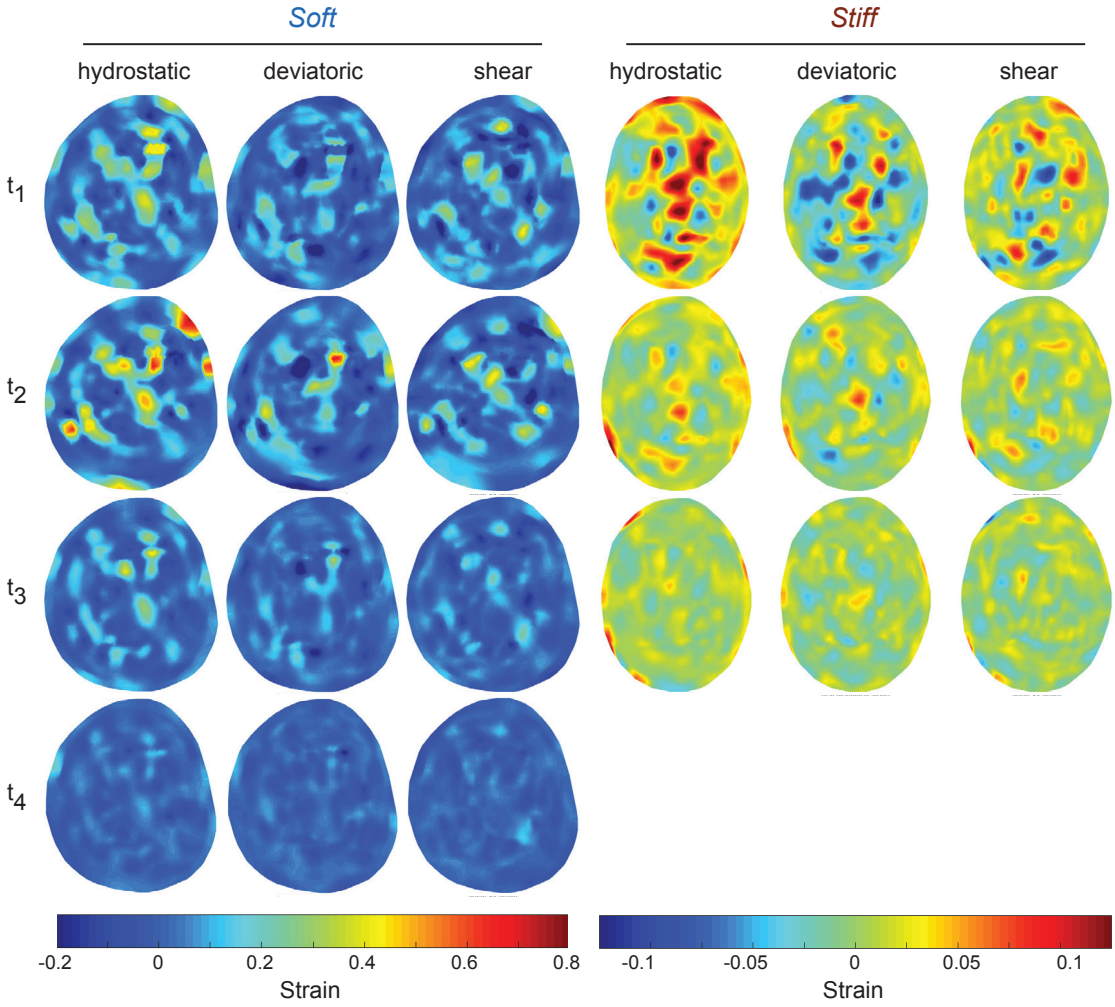

Figure 5. Intranuclear Strain Maps over Time during Cardiomyocyte Contraction in Physiological or Pathological Mechanical Environments
Cardiomyocytes expressing H2b-EGFP were plated on soft (~12 kPa, physiological) or stiff (~434 kPa, pathological) PDMS substrates. Image stacks of nuclear deformation during contraction were recorded and intranuclear strain maps were generated via deformation microscopy, using the diastolic resting state as the undeformed template, for different time steps during contraction (t_1, t_2, t_3, t_4). These data represent the detailed time course of intranuclear strain maps analyzed in Figures 4A and 4B.

change-related deviatoric strains showed low correlation with stress relaxation over time (R^2 = 0.12) or for different cells (R^2 = 0.41), and shear strains showed good correlation over time (R^2 = 0.97), but they were weakly correlated with different cells (R^2 = 0.22). These results were anticipated as cell dehydration is assumed to be equibiaxial, and therefore changes in volume, as represented by hydrostatic strain, should be dominant.

Finally, to demonstrate the benefits of computing spatial strain maps, we investigated whether a spatial relation existed between substrate stress relaxation and intranuclear hydrostatic strains. For this purpose, we generated a radial stress relaxation map, with values indicating the stress toward the nuclear center (Figure 6E). The radial stress relaxation at the cell border (10% of the outer nuclear area) was then plotted together with the hydrostatic strain at the nuclear border over the radial position relative to the nuclear center. Radial stress relaxation revealed three prominent peaks that coincided with the radial position of each cell apex. However, hydrostatic strain at the nuclear border showed a different trend, with a prominent peak (low compression) at the radial position of apex 2, but higher compression at apices 1 and 3. In addition, a peak was observed between apices 1 and 2 and more distinctly between apices 1 and 3 at the opposing radial position of apex 2. Because this result seemed puzzling at first, we also acquired a z stack of actin-stained P4 chondrocytes with a similar cell geometry. This revealed that the most prominent apex in a cell (e.g., apex 2) is distinct from the others in that it serves as the focal point for dorsal stress fibers that stretch over the nucleus and connect to ventral stress fibers on the opposite side that connect to apices 1 and 3 (Figure 6F). Based on these observations, we postulated a model in which dorsal actin fibers maintain nuclear tension along the primary apex axes (through LINC complex connections), while the collapse of the ventral actin fiber network cannot provide structural support and result in higher compression of the

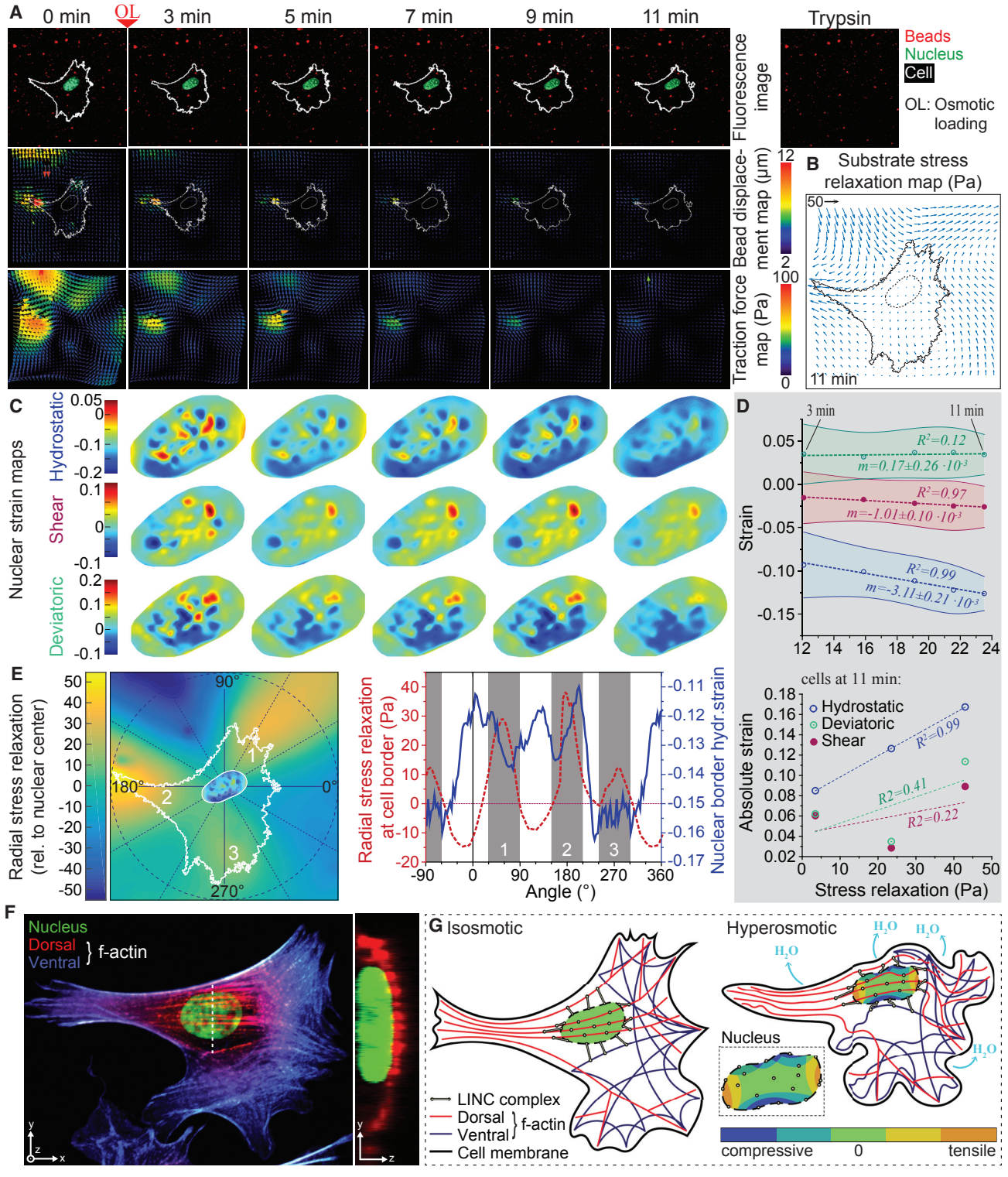

Figure 6. Cytoskeletal Geometry during Hyperosmotic Loading of Chondrocytes Leads to Nuclear Strain Asymmetry, as Detected through a Combined Analysis of Deformation Microscopy and Traction Force Microscopy

(A) Cells (outline = white, nuclei = green) cultured on PDMS with embedded fluorescent beads (red) shrink due to hyperosmotic loading. Bead displacement and traction force maps over time were quantified using a reference image obtained after cells were released through trypsin treatment (Trypsin); scale, 20 μm.

(B) Substrate stress relaxation map at 11 min was calculated using the traction force map before hyperosmotic loading (0 min) as a reference.

(legend continued on next page)

nucleus at these positions (Figure 6G). These results confirmed that deformation microscopy can generate nuclear strain maps that are sensitive to the applied loading mode, as hydrostatic strains were found to be dominant during equibiaxial cell shrinkage. Furthermore, this work demonstrates how spatial strain maps can be used in conjunction with spatial data from other methods, such as traction force microscopy, to reveal greater insight into nuclear mechanics.

DISCUSSION

Deformation microscopy enables detailed, spatially dependent investigations of the cell and nucleus interior in a broad range of physiological and disease applications. The development of deformation microscopy leverages conventional imaging and an automated hyperelastic warping algorithm to investigate strain history, deformation dynamics, and changes in structural heterogeneity within the interior of cells and nuclei. Deformation microscopy represents a foundational approach toward intracellular elastography and can provide quantitative insights into diverse mechanobiological applications. The technique can be applied to data from any image modality and only requires sufficient "texture" in images representing critical subcellular structures (e.g., actin stress fiber or chromatin architecture within cells). Reliable spatial registration map generation is only limited by the imaging quality.

Deformation microscopy is automated and valid for both 2D and 3D imaging modalities (Henderson et al., 2013). Accordingly, the derived parameters (in this case, strain) can be quantified in 2D as well as in 3D. The automated, unbiased optimization capability in the present technique ensures repeatability and makes the technique user-independent. Therefore, the present technique is a significant advancement over our previous work (Henderson et al., 2013), which required an experienced user to provide judgment to set the optimization parameters. In the present study, we also intentionally used only cell models grown in 2D environments with the assumption that strains in the z direction will be negligible for such cases. However, extension to 3D is easily possible at a cost of increased computational demand and may be best used when known spatial gradients exist across the nucleus, including variations of tension on lamins across the nuclear surface (Ihalainen et al., 2015), or when possible, spatial gradients are suspected or completely unknown.

Our model assumes a hyperelastic material model, which is justified by the results of previous studies. Hyperelasticity encompasses a large class of material models, including complex and nonlinear elasticity, and enables description of intracellular deformation for most applications. For the nucleus, very high strain occurs in a few scenarios such as migration of cancer cells through constrictions (Denais et al., 2016), which then recover after passing through the constriction, thus still showing hyperelastic and not plastic or permanent deformation behavior. For most applications of nuclear mechanics, the deformation is relatively low or recovers quickly over time. Viscoelastic or time-dependent behavior of the nucleus has also been investigated in isolated cells and nuclei. It was found from two independent studies that the nucleus does show viscoelastic behavior at the verge of a suddenly applied deformation (Guilak et al., 2000; Guilluy et al., 2014). After a short stabilization period, the nucleus behaves as an elastic solid. These studies induced sudden deformation on nuclei using micropipette aspiration or bead displacement. *In vivo*, sudden deformation on nuclei rarely happens and thus, an elastic material model can be appropriate. Because biological materials often also display time-dependent viscoelastic behavior, as well as plastic behavior at very large deformations, mechanical characterization of these materials is still possible via deformation microscopy through the acquisition of time course data.

Our technique can be used to gain mechanistic insight into nuclear mechanics with compromised structural elements. Disrupting all LINC complex connections through the overexpression of a truncated KASH construct abrogated nuclear force transmission as has been shown before (Lombardi and Lammerding, 2011). The knock down of nesprin-3 alone led to an almost equally strong alteration in nuclear mechanics. The roles of nesprins in cell biology are still being discovered. Of the four types of nesprins, nesprins 1 and 2 are mostly investigated in the context of nuclear mechanics and mechanobiology (Isermann and Lammerding, 2013). The loss of nesprins 1 and 2 is known to be responsible for several diseases, including Emery-Dreifuss muscular dystrophy and dilated cardiomyopathy. The loss of nesprin-4 is related to hearing loss. No disease has been reported so far in which nesprin-3 is compromised, and nesprin-3 knockouts show no distinctive phenotype (Zhang et al., 2009; Ketema et al., 2013). However, the ubiquitously conserved nature of nesprin-3 also shows how important nesprin-3 is to fundamental biological processes. In endothelial cells, nesprins are known to play an important role in the response to fluid shear stress, with the depletion of nesprin-3 causing altered cell morphology and impaired cell polarization and migration in the direction of the fluid flow (Morgan et al., 2011). Another

(C) Hydrostatic, shear, and deviatoric nuclear strain maps show that hydrostatic strains become more compressive over time.
(D) Top: correlation of average nuclear strains with average substrate stress relaxation at different time points during hyperosmotic loading. Bottom: correlation of nuclear strains with average substrate stress relaxation cells at the endpoint of hyperosmotic loading (11 min). Hydrostatic strains showed the highest correlation in both cases; n = 3, areas = SD.
(E) Left: the radial stress relaxation map was calculated from (B) by recalculating the magnitude with respect to the nuclear center. The nucleus inlay shows hydrostatic strain at 11 min, the white outline indicates the cell boundary, and the white numbers represent cell apices. Right: simultaneous plotting of radial stress relaxation of the substrate at the cell boundary and hydrostatic strain at the nuclear border over their radial position with respect to the nuclear center.
(F) Confocal z stack of a stained P4 chondrocyte. Actin staining has been split into two regions, depending on the z location: lower z (ventral, blue) and higher z (dorsal, red). The white dotted line indicates the position of the yz projection on the right. Dorsal stress fibers from the primary apex stretch over the nucleus, while ventral ones do not.
(G) Model of the observed nuclear hydrostatic strain during hyperosmotic loading. Strain patterns in (E) indicate a difference in the strain pattern along the primary apex 2 versus secondary apices 1 and 3. Primary apex-associated dorsal stress fibers keep the nucleus aligned along the apex axis, resulting in lower compression, while the collapse of ventral stress fibers may contribute to higher nuclear compression at the secondary apex locations.

investigative group demonstrated that the actomyosin, nesprin-3, and vimentin cooperatively move the nucleus like a piston during 3D migration (Petrie et al., 2014). Therefore, the role of nesprin-3 in nuclear mechanics is increasingly important, and we demonstrated here that the lack of nesprin-3 abrogates nuclear strain transfer in cardiomyocytes.

In addition to gaining insight into strain transfer through the LINC complex, our deformation microscopy technique was also used to elucidate the role of lamin A/C in strain propagation to the nucleus *in vivo*. The lack of lamin A/C is involved in numerous diseases, collectively known as laminopathies (Isermann and Lammerding, 2013). The compromise in lamin A/C is known to cause abnormal nuclear mechanics and phenotypes (Lammerding et al., 2004). Previous *in vitro* experiments report a softer nucleus due to lamin A/C deficiency that can lead to higher strain transfer to the nucleus (Zwerger et al., 2017), while other studies suggest stiffer nuclei in lamin A/C-deficient cells (Lanzicher et al., 2015). Our *in vivo* studies show a decreased strain inside the nuclei of skeletal muscle, which suggests a potential stiffening of the nucleus within the tissue of living animals. It is important to consider that a full analysis of nuclear stiffness requires a careful consideration of nuclear boundary (e.g., membrane) forces, and stiffness cannot be directly inferred from strain data alone. It should be noted that we observed only a minor decline of nuclear strain in hemizygote mice ($Lmna^{+/-}$) compared to wild-type mice ($Lmna^{+/+}$). Hemizygote mice were shown to manifest defects in cardiac physiology (Wolf et al., 2008; Cupesi et al., 2010). Although our experimental system is skeletal muscle, and hemizygote mice nuclear strain is comparable to wild-type mice nuclear strain, there may still be a possibility that skeletal muscles are functionally affected in hemizygote mice. Further studies are warranted to explore such possibilities.

To further show the potential of our technique, we provided a differential nuclear strain analysis for cardiomyocytes in different mechanical environments to support the hypothesis that nuclear mechanosensation is linked to the beating decline of cardiomyocytes on stiffer substrates. It has been shown that locally applied strains, particularly shear and hydrostatic strain, are sufficient to alter the expression of genes without any other influence (Tajik et al., 2016). It is also known that the activity of a gene is related to its compaction state, which is orchestrated by epigenetic modifications, defined by the changes in organisms caused by the modification of gene expression rather than alteration of the genetic code itself (Lawrence et al., 2016). For example, methylations of different histone residues can inactivate genes that were important during development but are locked away in the adult stage. Cardiac performance declines in conditions such as hypertrophy, ischemia, hypoxia, and atrophy, and these conditions have long been related to the reactivation of fetal gene networks (Cox and Marsh, 2014). If we further consider that dense chromatin mainly comprises silenced heterochromatin, then we can postulate that the elevated discrepancy in strain for dense chromatin areas for cells plated on soft versus stiff substrates, as observed in the present study, could have a profound impact on epigenetic controls and therefore contribute to the reactivation of silenced genes in these areas. These results form a strong basis to further investigate the effects of altered nuclear mechanics on chromatin organization, not only in heart disease but also in many other conditions that are marked by dramatic changes in mechanical properties of the respective tissues (e.g., diverse fibrotic conditions in the brain or liver, osteoarthritis in joint tissues, cancer).

We also demonstrated that deformation microscopy, in combination with other established microscale measurement techniques, can provide interesting mechanical insights that are not available from the use of either technique alone. In this study, we combined our technique with traction force microscopy to spatially correlate forces applied by chondrocytes onto their substrate with intranuclear strains during hyperosmotic loading. Based on these experimental observations, we proposed a simple model (Figure 6G) in which dorsal actin fibers, as in apex 2, keep the nucleus stretched along the fiber direction (through LINC complex connections), while the collapse of the ventral actin fiber network cannot provide structural support for the nucleus in the radial direction of apices 1 and 3. Collapsed ventral actin fibers along the secondary apices may even contribute to the higher compression observed at their radial positions. Of course, this model neglects other cytoskeleton and physical components that may have an influence on nuclear strains during the collapse. However, it is important to note that chondrocytes in their native 3D cartilage environment have a sphere-shaped constellation, including a spherical actin cytoskeleton that encloses the nucleus. Thus, our model already provides a meaningful explanation for how a spherical actin skeleton prevents local nuclear disturbances during osmotic challenges (e.g., during walking), as observed in the 2D cultures, thereby highlighting the importance of this native 3D spherical confirmation and the need to study chondrocyte mechanosensation in their native environment.

Lastly, as another application, we conducted intranuclear strain measurements during the spreading of chondrocytes (Figure S6). With ongoing cell spreading, an increasingly compressive trend was observed for hydrostatic strain patterns, while shear and deviatoric strains remained mostly unchanged. This was anticipated, as cell spreading can be assumed to be equibiaxial, and hence changes in volume (as represented by hydrostatic strain) should be dominant.

In conclusion, deformation microscopy provides a powerful tool to evaluate intracellular and intranuclear patterns of displacement and strain that relate to the distributions of mechanical force through distinct subcellular architectures. This method is neither restricted to the nucleus nor to *in vitro* cultures, but can be used over a wide spatial range, including cells and tissues *in vivo*, as long as image acquisition is sufficient to provide unique features that can be tracked in image sequences. In combination with other quantitative biological techniques, deformation microscopy can enable the spatial description of mechanical parameters (i.e., elastography) and be applied to a broad range of mechanobiological applications.

STAR★METHODS

Detailed methods are provided in the online version of this paper and include the following:

- KEY RESOURCES TABLE
- CONTACT FOR REAGENT AND RESOURCE SHARING

SUPPLEMENTAL INFORMATION

Supplemental Information can be found online at https://doi.org/10.1016/j.celrep.2019.04.009.

ACKNOWLEDGMENTS

We thank Jessica Kelly for technical assistance. This work was supported in part by NIH grants R01 AR063712 and R21 AR066230 and NSF grant CMMI CAREER 1349735.

AUTHOR CONTRIBUTIONS

All of the authors conceived the study, designed the experiments, and reviewed the manuscript. S.G., B.S., J.T.H., A.K.S., and R.D.W. performed the experiments. S.G., B.S., and J.T.H. carried out the data analysis. S.G., B.S., and C.P.N. wrote the manuscript.

DECLARATION OF INTERESTS

The authors declare no competing interests.

Received: August 31, 2018
Revised: January 10, 2019
Accepted: April 1, 2019
Published: April 30, 2019

REFERENCES

Alam, S.G., Zhang, Q., Prasad, N., Li, Y., Chamala, S., Kuchibhotla, R., Kc, B., Aggarwal, V., Shrestha, S., Jones, A.L., et al. (2016). The mammalian LINC complex regulates genome transcriptional responses to substrate rigidity. Sci. Rep. *6*, 38063.

Banerjee, I., Zhang, J., Moore-Morris, T., Pfeiffer, E., Buchholz, K.S., Liu, A., Ouyang, K., Stroud, M.J., Gerace, L., Evans, S.M., et al. (2014). Targeted ablation of nesprin 1 and nesprin 2 from murine myocardium results in cardiomyopathy, altered nuclear morphology and inhibition of the biomechanical gene response. PLoS Genet. *10*, e1004114.

Brock, K.K., Sharpe, M.B., Dawson, L.A., Kim, S.M., and Jaffray, D.A. (2005). Accuracy of finite element model-based multi-organ deformable image registration. Med. Phys. *32*, 1647–1659.

Califano, J.P., and Reinhart-King, C.A. (2010). Substrate stiffness and cell area predict cellular traction stresses in single cells and cells in contact. Cell. Mol. Bioeng. *3*, 68–75.

Cox, E.J., and Marsh, S.A. (2014). A systematic review of fetal genes as biomarkers of cardiac hypertrophy in rodent models of diabetes. PLoS One *9*, e92903.

Crisp, M., Liu, Q., Roux, K., Rattner, J.B., Shanahan, C., Burke, B., Stahl, P.D., and Hodzic, D. (2006). Coupling of the nucleus and cytoplasm: role of the LINC complex. J. Cell Biol. *172*, 41–53.

Cupesi, M., Yoshioka, J., Gannon, J., Kudinova, A., Stewart, C.L., and Lammerding, J. (2010). Attenuated hypertrophic response to pressure overload in a lamin A/C haploinsufficiency mouse. J. Mol. Cell. Cardiol. *48*, 1290–1297.

Denais, C.M., Gilbert, R.M., Isermann, P., McGregor, A.L., te Lindert, M., Weigelin, B., Davidson, P.M., Friedl, P., Wolf, K., and Lammerding, J. (2016). Nuclear envelope rupture and repair during cancer cell migration. Science *352*, 353–358.

Dingal, P.C.D.P., Bradshaw, A.M., Cho, S., Raab, M., Buxboim, A., Swift, J., and Discher, D.E. (2015). Fractal heterogeneity in minimal matrix models of scars modulates stiff-niche stem-cell responses via nuclear exit of a mechanorepressor. Nat. Mater. *14*, 951–960.

Driscoll, T.P., Cosgrove, B.D., Heo, S.J., Shurden, Z.E., and Mauck, R.L. (2015). Cytoskeletal to Nuclear Strain Transfer Regulates YAP Signaling in Mesenchymal Stem Cells. Biophys. J. *108*, 2783–2793.

Engler, A.J., Carag-Krieger, C., Johnson, C.P., Raab, M., Tang, H.Y., Speicher, D.W., Sanger, J.W., Sanger, J.M., and Discher, D.E. (2008). Embryonic cardiomyocytes beat best on a matrix with heart-like elasticity: scar-like rigidity inhibits beating. J. Cell Sci. *121*, 3794–3802.

Fan, D., Takawale, A., Lee, J., and Kassiri, Z. (2012). Cardiac fibroblasts, fibrosis and extracellular matrix remodeling in heart disease. Fibrogenesis Tissue Repair *5*, 15.

Ghosh, S., Cimino, J.G., Scott, A.K., Damen, F.W., Phillips, E.H., Veress, A.I., Neu, C.P., and Goergen, C.J. (2017). In vivo multiscale and spatially-dependent biomechanics reveals differential strain transfer hierarchy in skeletal muscle. ACS Biomater. Sci. Eng. *3*, 2798–2805.

Gilchrist, C.L., Witvoet-Braam, S.W., Guilak, F., and Setton, L.A. (2007). Measurement of intracellular strain on deformable substrates with texture correlation. J. Biomech. *40*, 786–794.

Grady, R.M., Starr, D.A., Ackerman, G.L., Sanes, J.R., and Han, M. (2005). Syne proteins anchor muscle nuclei at the neuromuscular junction. Proc. Natl. Acad. Sci. USA *102*, 4359–4364.

Guilak, F., Tedrow, J.R., and Burgkart, R. (2000). Viscoelastic properties of the cell nucleus. Biochem. Biophys. Res. Commun. *269*, 781–786.

Guilluy, C., Osborne, L.D., Van Landeghem, L., Sharek, L., Superfine, R., Garcia-Mata, R., and Burridge, K. (2014). Isolated nuclei adapt to force and reveal a mechanotransduction pathway in the nucleus. Nat. Cell Biol. *16*, 376–381.

Henderson, J.T., Shannon, G., Veress, A.I., and Neu, C.P. (2013). Direct measurement of intranuclear strain distributions and RNA synthesis in single cells embedded within native tissue. Biophys. J. *105*, 2252–2261.

Heo, S.J., Thorpe, S.D., Driscoll, T.P., Duncan, R.L., Lee, D.A., and Mauck, R.L. (2015). Biophysical regulation of chromatin architecture instills a mechanical memory in mesenchymal stem cells. Sci. Rep. *5*, 16895.

Ihalainen, T.O., Aires, L., Herzog, F.A., Schwartlander, R., Moeller, J., and Vogel, V. (2015). Differential basal-to-apical accessibility of lamin A/C epitopes in the nuclear lamina regulated by changes in cytoskeletal tension. Nat. Mater. *14*, 1252–1261.

Isermann, P., and Lammerding, J. (2013). Nuclear mechanics and mechanotransduction in health and disease. Curr. Biol. *23*, R1113–R1121.

Iskratsch, T., Wolfenson, H., and Sheetz, M.P. (2014). Appreciating force and shape—the rise of mechanotransduction in cell biology. Nat. Rev. Mol. Cell Biol. *15*, 825–833.

Iyer, K.V., Pulford, S., Mogilner, A., and Shivashankar, G.V. (2012). Mechanical activation of cells induces chromatin remodeling preceding MKL nuclear transport. Biophys. J. *103*, 1416–1428.

Joffe, B., Leonhardt, H., and Solovei, I. (2010). Differentiation and large scale spatial organization of the genome. Curr. Opin. Genet. Dev. *20*, 562–569.

Johnston, I.D., McCluskey, D.K., Tan, C.K.L., and Tracey, M.C. (2014). Mechanical characterization of bulk Sylgard 184 for microfluidics and microengineering. J. Micromech. Microeng. *24*, 035017.

Ketema, M., Kreft, M., Secades, P., Janssen, H., and Sonnenberg, A. (2013). Nesprin-3 connects plectin and vimentin to the nuclear envelope of Sertoli cells but is not required for Sertoli cell function in spermatogenesis. Mol. Biol. Cell *24*, 2454–2466.

Knight, M.M., van de Breevaart Bravenboer, J., Lee, D.A., van Osch, G.J., Weinans, H., and Bader, D.L. (2002). Cell and nucleus deformation in compressed chondrocyte-alginate constructs: temporal changes and calculation of cell modulus. Biochim. Biophys. Acta *1570*, 1–8.

Lammerding, J., Schulze, P.C., Takahashi, T., Kozlov, S., Sullivan, T., Kamm, R.D., Stewart, C.L., and Lee, R.T. (2004). Lamin A/C deficiency causes defective nuclear mechanics and mechanotransduction. J. Clin. Invest. *113*, 370–378.

Lanzicher, T., Martinelli, V., Long, C.S., Del Favero, G., Puzzi, L., Borelli, M., Mestroni, L., Taylor, M.R., and Sbaizero, O. (2015). AFM single-cell force spectroscopy links altered nuclear and cytoskeletal mechanics to defective cell adhesion in cardiac myocytes with a nuclear lamin mutation. Nucleus *6*, 394–407.

Lawrence, M., Daujat, S., and Schneider, R. (2016). Lateral Thinking: How Histone Modifications Regulate Gene Expression. Trends Genet. *32*, 42–56.

Lombardi, M.L., and Lammerding, J. (2011). Keeping the LINC: the importance of nucleocytoskeletal coupling in intracellular force transmission and cellular function. Biochem. Soc. Trans. *39*, 1729–1734.

Mann, J.M., Lam, R.H., Weng, S., Sun, Y., and Fu, J. (2012). A silicone-based stretchable micropost array membrane for monitoring live-cell subcellular cytoskeletal response. Lab Chip *12*, 731–740.

Martiel, J.-L., Leal, A., Kurzawa, L., Balland, M., Wang, I., Vignaud, T., Tseng, Q., and Théry, M. (2015). Measurement of cell traction forces with ImageJ. Methods Cell Biol. *125*, 269–287.

Morgan, J.T., Pfeiffer, E.R., Thirkill, T.L., Kumar, P., Peng, G., Fridolfsson, H.N., Douglas, G.C., Starr, D.A., and Barakat, A.I. (2011). Nesprin-3 regulates endothelial cell morphology, perinuclear cytoskeletal architecture, and flow-induced polarization. Mol. Biol. Cell *22*, 4324–4334.

Neu, C.P., Khalafi, A., Komvopoulos, K., Schmid, T.M., and Reddi, A.H. (2007). Mechanotransduction of bovine articular cartilage superficial zone protein by transforming growth factor beta signaling. Arthritis Rheum. *56*, 3706–3714.

Neu, C.P., Reddi, A.H., Komvopoulos, K., Schmid, T.M., and Di Cesare, P.E. (2010). Increased friction coefficient and superficial zone protein expression in patients with advanced osteoarthritis. Arthritis Rheum. *62*, 2680–2687.

Peffers, M.J., Milner, P.I., Tew, S.R., and Clegg, P.D. (2010). Regulation of SOX9 in normal and osteoarthritic equine articular chondrocytes by hyperosmotic loading. Osteoarthritis Cartilage *18*, 1502–1508.

Petrie, R.J., Koo, H., and Yamada, K.M. (2014). Generation of compartmentalized pressure by a nuclear piston governs cell motility in a 3D matrix. Science *345*, 1062–1065.

Pombo, A., and Dillon, N. (2015). Three-dimensional genome architecture: players and mechanisms. Nat. Rev. Mol. Cell Biol. *16*, 245–257.

Raab, M., Gentili, M., de Belly, H., Thiam, H.R., Vargas, P., Jimenez, A.J., Lautenschlaeger, F., Voituriez, R., Lennon-Duménil, A.M., Manel, N., and Piel, M. (2016). ESCRT III repairs nuclear envelope ruptures during cell migration to limit DNA damage and cell death. Science *352*, 359–362.

Sarantitis, I., Papanastasopoulos, P., Manousi, M., Baikossis, N.G., and Apostolakis, E. (2012). The cytoskeleton of the cardiac muscle cell. Hellenic J. Cardiol. *53*, 367–379.

Seelbinder, B., Ghosh, S., Berman, A.G., Schneider, S.E., Goergen, C.J., Calve, S., and Neu, C.P. (2018). The nucleus mediates mechanosensitive reorganization of epigenetically marked chromatin during cardiac maturation and pathology. bioRxiv. https://doi.org/10.1101/455600.

Solovei, I., Wang, A.S., Thanisch, K., Schmidt, C.S., Krebs, S., Zwerger, M., Cohen, T.V., Devys, D., Foisner, R., Peichl, L., et al. (2013). LBR and lamin A/C sequentially tether peripheral heterochromatin and inversely regulate differentiation. Cell *152*, 584–598.

Stroud, M.J., Banerjee, I., Veevers, J., and Chen, J. (2014). Linker of nucleoskeleton and cytoskeleton complex proteins in cardiac structure, function, and disease. Circ. Res. *114*, 538–548.

Swift, J., and Discher, D.E. (2014). The nuclear lamina is mechano-responsive to ECM elasticity in mature tissue. J. Cell Sci. *127*, 3005–3015.

Taimen, P., Pfleghaar, K., Shimi, T., Möller, D., Ben-Harush, K., Erdos, M.R., Adam, S.A., Herrmann, H., Medalia, O., Collins, F.S., et al. (2009). A progeria mutation reveals functions for lamin A in nuclear assembly, architecture, and chromosome organization. Proc. Natl. Acad. Sci. USA *106*, 20788–20793.

Tajik, A., Zhang, Y., Wei, F., Sun, J., Jia, Q., Zhou, W., Singh, R., Khanna, N., Belmont, A.S., and Wang, N. (2016). Transcription upregulation via force-induced direct stretching of chromatin. Nat. Mater. *15*, 1287–1296.

Talwar, S., Kumar, A., Rao, M., Menon, G.I., and Shivashankar, G.V. (2013). Correlated spatio-temporal fluctuations in chromatin compaction states characterize stem cells. Biophys. J. *104*, 553–564.

Taranum, S., Vaylann, E., Meinke, P., Abraham, S., Yang, L., Neumann, S., Karakesisoglou, I., Wehnert, M., and Noegel, A.A. (2012). LINC complex alterations in DMD and EDMD/CMT fibroblasts. Eur. J. Cell Biol. *91*, 614–628.

Veress, A., Phatak, N., and Weiss, J.A. (2004). Deformable Image Registration with Hyperelastic Warping. In Handbook of Biomedical Image Analysis, Vol. III: Registration Models, J.S. Suri, D.L. Wilson, and S. Laxminarayan, eds. (Springer), pp. 487–534.

Wang, N., Tytell, J.D., and Ingber, D.E. (2009). Mechanotransduction at a distance: mechanically coupling the extracellular matrix with the nucleus. Nat. Rev. Mol. Cell Biol. *10*, 75–82.

Wilkie, G.S., Korfali, N., Swanson, S.K., Malik, P., Srsen, V., Batrakou, D.G., de las Heras, J., Zuleger, N., Kerr, A.R., Florens, L., and Schirmer, E.C. (2011). Several Novel Nuclear Envelope Transmembrane Proteins Identified in Skeletal Muscle Have Cytoskeletal Associations. Mol. Cell Proteomics *10*, M110.003129.

Wojcik, K., and Dobrucki, J.W. (2008). Interaction of a DNA intercalator DRAQ5, and a minor groove binder SYTO17, with chromatin in live cells–influence on chromatin organization and histone-DNA interactions. Cytometry A *73*, 555–562.

Wolf, C.M., Wang, L., Alcalai, R., Pizard, A., Burgon, P.G., Ahmad, F., Sherwood, M., Branco, D.M., Wakimoto, H., Fishman, G.I., et al. (2008). Lamin A/C haploinsufficiency causes dilated cardiomyopathy and apoptosis-triggered cardiac conduction system disease. J. Mol. Cell. Cardiol. *44*, 293–303.

Wu, P.-H., Aroush, D.R., Asnacios, A., Chen, W.C., Dokukin, M.E., Doss, B.L., Durand-Smet, P., Ekpenyong, A., Guck, J., Guz, N.V., et al. (2018). A comparison of methods to assess cell mechanical properties. Nat. Methods *15*, 491–498.

Zhang, X., Lei, K., Yuan, X., Wu, X., Zhuang, Y., Xu, T., Xu, R., and Han, M. (2009). SUN1/2 and Syne/Nesprin-1/2 complexes connect centrosome to the nucleus during neurogenesis and neuronal migration in mice. Neuron *64*, 173–187.

Zuleger, N., Boyle, S., Kelly, D.A., de las Heras, J.I., Lazou, V., Korfali, N., Batrakou, D.G., Randles, K.N., Morris, G.E., Harrison, D.J., et al. (2013). Specific nuclear envelope transmembrane proteins can promote the location of chromosomes to and from the nuclear periphery. Genome Biol. *14*, R14.

Zwerger, M., Jaalouk, D.E., Lombardi, M.L., Isermann, P., Mauermann, M., Dialynas, G., Herrmann, H., Wallrath, L.L., and Lammerding, J. (2017). Myopathic lamin mutations impair nuclear stability in cells and tissue and disrupt nucleocytoskeletal coupling. Hum. Mol. Genet. *22*, 2335–2349.

STAR★METHODS

KEY RESOURCES TABLE

REAGENT or RESOURCE	SOURCE	IDENTIFIER
Antibodies		
anti-nesprin-1	Abcam	ab24742
Goat anti-Rabbit IgG – Alexa Fluor 633	ThermoFisher	A-21071
Chemicals, Peptides, and Recombinant Proteins		
GIBCO Trypsin-EDTA (0.5%), No Phenol Red	ThermoFisher	15400054
Geltrex Matrigel	ThermoFisher	A1413201
Sylgard™ 527	Dow	1673564
Sylgard™ 184	Dow	1317318
Lenti-X Packaging Single Shots	Takara Bio	631278
Advanced DMEM/F12	ThermoFisher	12634010
EMS 32% Paraformaldehyde aqueous solution	ThermoFisher	50980495
Tween 20	Sigma-Aldrich	P1379
NucBlue™ Live ReadyProbes™ Reagent	ThermoFisher	R37605
TrypLE Express Enzyme (1X), phenol red	ThermoFisher	12605010
Fibronectin bovine plasma	Sigma-Aldrich	F1141
Fetal Bovine Serum, certified	ThermoFisher	16000036
Hoechst 33342, Trihydrochloride, Trihydrate - 10 mg/mL Solution in Water	ThermoFisher	H3570
FluoSpheres Carboxylate-Modified Microspheres, 0.5 μm, red fluorescent (580/605), 2% solids	ThermoFisher	F8812
DRAQ5	Cell Signaling Technology	4084
Critical Commercial Assays		
Aurum™ Total RNA Mini Kit	Bio-Rad	7326820
iScript™ Reverse Transcription Supermix for RT-qPCR	Bio-Rad	1708840
SsoAdvanced™ Universal SYBR® Green Supermix	Bio-Rad	1725270
Experimental Models: Cell		
Chondrocytes harvested from young bovines	Local vendor	N/A
Experimental Models: Organisms/Strains		
B6.Cg-Tg (HIST1H2BB/EGFP) 1Pa/J mice	Jackson Laboratory	006069
B6129S1(Cg)-*Lmna*^{tm1Stw}/BkknJ	Jackson Laboratory	009125
Software and Algorithms		
MATLAB	MathWorks	N/A
ANSYS	ANSYS	N/A
nike3D	Lawrence Livermore National Lab	N/A
TrueGrid	XYZ Scientific Applications	N/A
WarpLab	University of Utah Musculoskeletal Research Laboratories	N/A
LS-PrePost	Livermore Software Technology Corp.	N/A
Other		
Nikon Ti-Eclipse inverted epi-fluorescence microscope	Nikon	N/A
Nikon Eclipse Ti-A1R inverted confocal microscope	Nikon	N/A
Olympus IX 73 inverted confocal microscope	Olympus	N/A
Olympus two photon microscope	Olympus	N/A
EMCCD Camera	Andor	N/A
5500 Atomic Force Microscope	Keysight Technologies	N/A
CFX96 Touch thermocycler	Bio-Rad	N/A

CONTACT FOR REAGENT AND RESOURCE SHARING

Further information and requests for resources and reagents should be directed to and will be fulfilled by the Lead Contact, Corey P. Neu (cpneu@colorado.edu).

EXPERIMENTAL MODEL AND SUBJECT DETAILS

Animal procedures were performed following Institutional Animal Care & Use Committee (IACUC) approved protocols.

Animals for cardiomyocyte experiments

B6.Cg-Tg (HIST1H2BB/EGFP) 1Pa/J mice were obtained from Jackson Laboratory (#006069).

Lamin A/C deficient mice

B6129S1(Cg)-*Lmna*^{tm1Stw}/BkknJ mice were purchased from Jackson Laboratory (#009125). Experiments were performed only on male mice.

Chondrocyte harvesting

Primary chondrocytes were harvested from the load-bearing region of the medial condyle from young female bovines.

METHOD DETAILS

Framework and validation of deformation microscopy

Deformation microscopy uses image acquisition and registration methods, and is based on the minimization of an energy functional, a function of space and deformation map which is the difference between the deformation-induced energy and the image comparison-based energy (Figure 1; Methods S1). In a basic two-dimensional implementation, *z*-projections of template (undeformed) and target (deformed) images are used to quantify local deformations (Figures 1A and S1). Confocal images of nuclei were used in the analysis to enable simulations and analysis in two-dimensions, although extension to three-dimensional analysis is possible (Henderson et al., 2013). Image data is prepared for a finite element analysis using meshing (to assign image points/nodes and elements), and the hyperelastic warping algorithm is applied to find the deformation map. A sequential spatial filter is applied to overcome the local image registration-driven premature registration (Methods S1). The deformation map can be used to generate various strain measures in the object of interest as suitable for the specific application, here demonstrated using the cell nucleus as an example (Methods S2). The material stiffness of the nucleus and the penalty factor are the two key parameters that are altered to find the best deformation map through optimization of the root mean square error (RMSE) of image pixel intensity derived from the template and the target images (Methods S2; Figure S1). A custom code (MATLAB) automated the process to measure intranuclear deformation. One set of calculations averaged 5-30 minutes, depending on the complexity of the specific application, including the spatial resolution and number of time steps. The calculated strain, which describes internal motion of the nucleus, and is not confounded by rigid body motion like translation and rotation, is presented as surface plots, with the heatmap scales defined by the upper and lower limit of the strain values.

Validation of deformation microscopy was determined using forward simulations of known deformations representative of motion expected in cellular systems. Representative images were obtained by confocal microscopy, and then were deformed using finite element software (ANSYS) to generate simulated deformation field data and deformed images. The simulated image data was also independently processed using deformation microscopy to generate (calculated) deformation data, which was compared to simulated data as a ground truth. Forward simulations included a sweep over a broad range of intranuclear material properties expected in biological systems (Methods S3; Figures 3, S2, and S3). Additionally, strain measures were described in terms of key descriptors and components, including hydrostatic, tensile, compressive, shear, and deviatoric strains, all of which help to characterize the complete description of internal motion (Figure 1C; Methods S2).

In vitro quantification of nuclear strains in cardiomyocytes

Cardiomyocyte Culture

B6.Cg-Tg (HIST1H2BB/EGFP) 1Pa/J mice were obtained from Jackson Laboratory (#006069). Homozygous mice were bred to maintain a homozygous population and all mice were weaned 21 days postnatal. Mice were housed in a temperature-controlled environment with a 12-hour light and dark cycle and allowed to graze for both food and water *ad libitum*. Cardiomyocytes were isolated from embryonic mice hearts 18.5 days post conception using cold trypsin digestion (incubation in 0.125% trypsin/EDTA overnight followed by 10 min digestion in residual trypsin under application of 37°C warm medium) and cultured on PDMS substrates (Sylgard®527, Dow Corning). The embryos harvested were a mixed population of males and females. Cardiomyocytes were cultured in Advanced DMEM/F12 containing 10% FBS at 37°C with 5% CO_2.

Substrate Fabrication

Polydimethylsiloxane (PDMS) substrates with different formulations were used to mimic physiological and pathological conditions: Sylgard®527 ratio 1:1 (E = 11.7 ± 5.4 kPa) and Sylgard®184 (Dow Corning) ratio 1:10 (E = 434.3 ± 54.4 kPa). PDMS Stiffness was determined via AFM (5500 Atomic Force Microscope, Keysight Technologies, Santa Rosa, CA, USA) using a spherical borosilicate glass tip (diameter = 10 μm, stiffness = 0.85 N/m), and Young's modulus E was calculated using a Hertz contact model. To enable live imaging at high magnification using a 100 × objective, thin (~80 μm) PDMS films were deposited on glass slides, degassed under vacuum for 30 min, cured for 2h at 100°C, and mounted on custom made cell culture dishes. PDMS was then ozone-treated and coated with Matrigel (Geltrex, ThermoFisher) for 1h at 37°C to complex cell attachment sites similar the cardiac basement membrane.

Imaging and Data Analysis

Image stacks of cardiomyocyte nuclei during contractions were captured using an inverted epi-fluorescence microscope (Nikon Ti-Eclipse) with a 100 × objective and an EMCCD camera (Andor). To visualize the entire contraction cycle of cardiomyocytes, images were captured at 6.4 fps over a period of 10 s, during which photobleaching was negligible. For each nucleus, one contraction cycle was selected from the image stack to perform nuclear deformation analysis. Images of the nuclei in a post-systolic resting state were selected as undeformed reference image. Chromatin density (H2b intensity) histograms could be fitted onto a 3-term Gaussian distribution and was rescaled to [-1 +1], with −1 being the lowest density, +1 the highest density and the histogram peak set to 0, to compare strain data from different nuclei.

Lentiviral Vectors and Transduction

The dominant negative TmKash3 construct contained the C-terminal end of the nesprin-3 gene (*Syne3*) including the transmembrane (Tm) and the KASH domain. The N terminus was replaced by a red fluorescence protein (mRuby3) for visual feedback and a signal peptide (SP, from *Tor1a*) for proper membrane integration. This truncated nesprin was designed to integrate into the outer nuclear membrane and compete with native nesprins for SUN connections via the KASH domain while lacking N-terminal cytoskeleton binding domains, therefore decoupling the nucleus (Grady et al., 2005). A control vector TmCtr was designed that was identical to the decoupling vector but lacked the KASH domain necessary for LINC complex integration. Lentiviral particles were produced using Lenti-X Packaging Single Shots (Takara Bio). For efficient transduction, particles where precipitated with 4mM $CaCl_2$ in Advanced DMEM/F12 (ThermoFisher) without serum and antibiotics for 1h at room temperature. After 24h of culture, cardiomyocytes were incubated in infectious medium for 2h.

Nesprin Immunostaining

Cells were fixed in 4% PFA for 10min, blocked with 10% NGS, 1% BSA in 0.1% PBT (0.1% Tween-20 in PBS) for 60min. Primary incubation was performed at 4°C overnight in 0.1% PBT containing 1% BSA using anti-nesprin-1 in a dilution of 1:500. Secondary incubation was performed in primary incubation buffer for 40min at room temperature at a dilution 1:500. Images were acquired on a Nikon A1R confocal microscope using a 60 × oil immersion objective.

Gene Expression Analysis

Total RNA was extracted from cardiomyocytes after four days of culture using Aurum™ Total RNA Mini Kit, reverse transcribed into cDNA via iScript™ Reverse Transcription Supermix and real-time quantitative PCR was performed with SsoAdvanced™ Universal SYBR® Green Supermix in a CFX96 Touch thermocycler (all kits and devices from Bio-Rad Laboratories) using 10 ng of cDNA per reaction. All data was normalized to the reference gene Gapdh. Primers were custom designed, and sequences are listed in Table S1.

In vivo quantification of nuclear strain transfer in skeletal muscles of Lamin A/C deficient mice

Lamin A/C deficient mice

B6129S1(Cg)-*Lmna*^{tm1Stw}/BkknJ mice were purchased from Jackson Laboratory (#009125). The targeted allele expresses a truncated Lamin A/C protein. Hemizygotes (*Lmna*$^{+/-}$) are viable and fertile. Subsequently the hemizygotes were bred to obtain the *Lmna*$^{+/+}$, *Lmna*$^{+/-}$, *Lmna*$^{-/-}$ mice. Homozygotes (*Lmna*$^{-/-}$ mice) exhibit severely retarded postnatal growth, beginning as early as 2 weeks of age, abnormal movement/gait by 3-4 weeks of age and die around 8 weeks of age. All mice were weaned 21 days postnatal. Mice were housed in a temperature-controlled environment with a 12-hour light and dark cycle and allowed to graze for both food and water *ad libitum*. Additionally, homozygotes (*Lmna*$^{-/-}$ mice) were provided DietGel Recovery (Clear H_2O).

Neuromuscular Stimulation

To quantify the nuclear strain-transfer in *in vivo* skeletal muscle we used neuromuscular stimulation as described previously (Ghosh et al., 2017). Briefly, anesthetized animals were kept in supine position and their gastrocnemius was exposed. Nuclei were stained by NucBlue™ Live ReadyProbes™ Reagent (ThermoFisher). The deep fibular nerve was stimulated to contract the gastrocnemius muscle and nuclei in the medial gastrocnemius were imaged before and after stimulation on an inverted confocal microscope (Nikon Eclipse Ti A1R) using a 40 × objective. Nuclear strains were then quantified using deformation microscopy.

Quantification of nuclear strains during hyperosmotic loading of chondrocytes

Chondrocyte Culture

Primary chondrocytes were harvested from the load-bearing region of the medial condyle from young bovines (Neu et al., 2007, 2010). Harvested cells were cultured in DMEM-F12 with 10% FBS (ThermoFisher) and passaged at around 80% confluency. The cells were maintained at 37°C with 5% CO_2.

Substrate Fabrication

Polydimethylsiloxane (PDMS; Sylgard®184, Dow Corning) was mixed at a ratio of 1:10 with 0.5 μm red fluorescent beads (ThermoFisher) and sandwiched between a Petri dish and a glass slide to gain thin and flat substrates. PDMS was degassed for 20 min, cured at 70°C for 12 h, and coated with 1μg/cm^2 fibronectin (Sigma-Aldrich) for 1 hour. Cells were plated at low density (i.e., maximum of ~5 to 9 cells per 106 × 106 μm^2) on substrates for 2 hours prior to hyperosmotic loading experiments.

Hyperosmotic Loading and Imaging

To create hyperosmotic conditions, culture media was removed, and saline solution was gently added to instantly increase the osmolality from 320 mOsm to 500 mOsm. Nuclei were labeled with Hoechst 33342 (ThermoFisher). Time-sequence images of nuclei and the substrates were captured one minute apart on an inverted confocal microscope (Olympus) using a 60 × water immersion objective. After 12 min, cells were detached from the substrate using TrypLE Express (ThermoFisher) and substrates were imaged again. A control experiment was conducted using the regular culture medium for the same time span as the hyperosmotic loading experiment.

Data analysis for traction force, stretching force on cell, and nuclear strain

The image sequence of the nuclei obtained from the hyperosmotic loading experiment was further analyzed to compute nuclear strain. A simple measure of bulk nuclear strain was obtained by fitting an ellipse to the nucleus and computing the change in major axis length. From the substrate images, traction force and substrate stress relaxation force on the cell was computed. Briefly, nuclear deformation was computed for each time point with respect to the first nuclear image (before application of osmotic loading) as the template. Traction forces at each time point were computed via the ImageJ-based PIV and traction force calculation plugin (Martiel et al., 2015) with reference to the last image after trypsin-mediated cell detachment. Substrate stress relaxation maps were computed by subtracting the traction force at the initial time point (0 min) from traction force maps at each time point (Mann et al., 2012). Young's modulus of the PDMS was estimated to be E = 1.76 MPa with a Poisson's ratio ν = 0.49 based on existing literature (Johnston et al., 2014).

QUANTIFICATION AND STATISTICAL ANALYSIS

One-way Analysis of Variance (ANOVA), followed by post hoc Tukey's test was used to test for statistically significant differences between treatment groups. The coefficient of determination (R^2) was calculated using linear regression. Error margins are reported as standard deviation (SD) or standard error of the mean (SEM), as indicated in the figure captions.

DATA AND SOFTWARE AVAILABILITY

Further information and requests for data, software and code should be directed to and will be fulfilled by the lead contact, Corey P. Neu (cpneu@colorado.edu).

ADDITIONAL RESOURCES

Passage 4 chondrocytes were derived as described in the chondrocyte hyperosmotic loading section. DNA of passage four bovine chondrocytes were stained in suspension with DRAQ5 (Cell Signaling) at concentration 0.5 μM. Chondrocytes were then plated on plastic dishes maintained at 37°C. Time-lapse images of the cells and nuclei were acquired using two-photon microscopy (Olympus with a tunable Mai-Tai laser set at 540-600 nm). See Figure S6A for details of the cell spreading. Intuitively, this simple cell spreading assay predicts a uniform strain pattern in the nucleus, as there is no directional loading applied on the cell. Bulk mechanical behavior of cell computed by cell aspect ratio and cell nuclear area follows this predictable pattern. Nucleus aspect ratio was nearly 1 (Figure S6B), suggesting a biaxial expansion and contraction during the time-course change of the nucleus area. However, the internal strain fields were locally complex, with spatiotemporal variations in tensile and compressive strain magnitudes, thus leading to complex hydrostatic and deviatoric strain (Figure S6C). From the spreading to anchoring phase, at some time points, high average tension (Figure S6D) was found, suggesting cells attach on the substrate via short protrusions. These results warrant further investigation of local nuclear behavior during cell spreading.

We included the cell adhesion assay using the stain DRAQ5, as another possible stain, because it is widely used as a live stain. However, it should be noted that at the higher concentration (> 1 μM) the DRAQ5 affects the reorganization of the chromatin and the nuclear biology. DRAQ5 is an intercalator and it affects the binding between histone and DNA. A study by Wojcik and Dobrucki specifically investigated this mechanism and reported that the effect of DRAQ5 on H2B is minimal, and more prominent on H1 (Wojcik and Dobrucki, 2008). While H2B is the part of the core histone octamer, the H1 links the nucleosome to the linker DNA. Therefore, DRAQ5 should affect the reorganization of the chromatin, but at a steady state the updated organization is stable and should not affect the mechanics, although gene expression pattern can change. However, this effect depends on the concentration of DRAQ5. At higher concentration (3 μM or higher) this effect is more prominent. We used a lower concentration (< 1 μM), for a short time to stain the chromatin after which the stain was washed for time-lapse microscopy. According to Wojcik and Dobrucki, at that concentration, the detectable changes in chromatin architecture is small, although not non-existent. At such a low concentration we get an inferior fluorescence and therefore we used a two-photon microscope to acquire the highest quality signal.

Cell Reports, Volume *27*

Supplemental Information

Deformation Microscopy for Dynamic Intracellular and Intranuclear Mapping of Mechanics with High Spatiotemporal Resolution

Soham Ghosh, Benjamin Seelbinder, Jonathan T. Henderson, Ryan D. Watts, Adrienne K. Scott, Alexander I. Veress, and Corey P. Neu

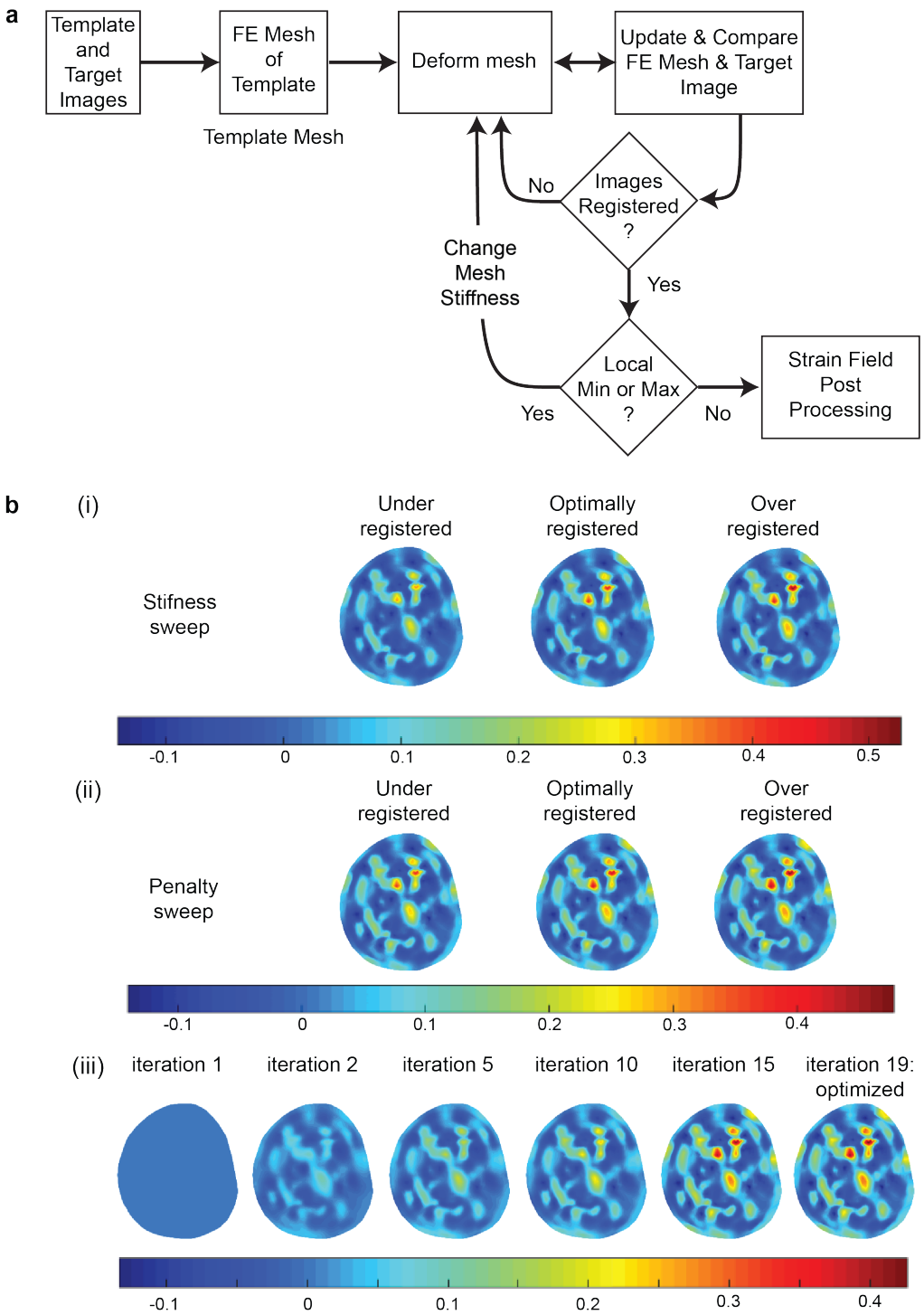

Figure S1. Flowchart and the details of image registration explaining iterative hyperelastic warping based deformable image registration, related to Figure 1. (a) The algorithm explains the technique step by step. The procedure is repeated with parameter (stiffness and penalty) sweep. **(b)** Demonstration of hydrostatic strain maps obtained by under-registration and over-registration of two parameters: stiffness (i) and penalty (ii). (iii) An optimal solution is reached by the iterative procedure after registration is achieved.

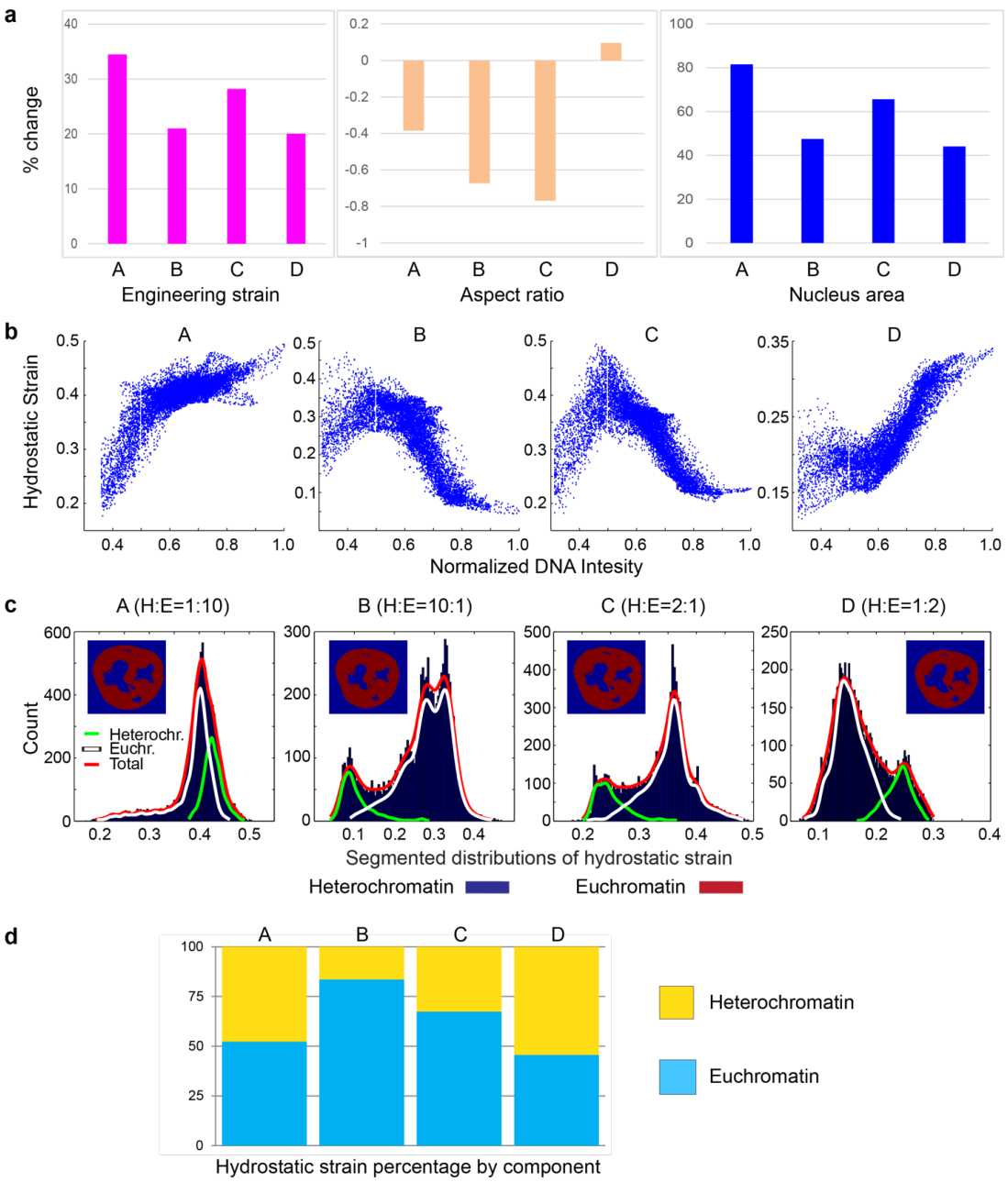

Figure S2. Effect of intranuclear stiffness on strain measurement, related to Figure 2. (a) Percent strain of the four nuclei, A, B, C and D, as measured by bulk measurements (i.e. engineering strain based on major axis, aspect ratio and nucleus area). **(b)** Hydrostatic strain vs. normalized chromatin intensity. For nuclei A and D, where the euchromatin region is stiffer, similar strain vs intensity trends were observed, with opposite trends found for nuclei B and C. **(c)** Segmentation of the nucleus images into euchromatin and heterochromatin regions show that the total strain distribution (blue histogram, highlighted with a red line) is a composite of the two strain distribution representing heterochromatin (green line) and euchromatin (white line). **(d)** Percentage of total hydrostatic strain distributed between the hetero- and euchromatin components.

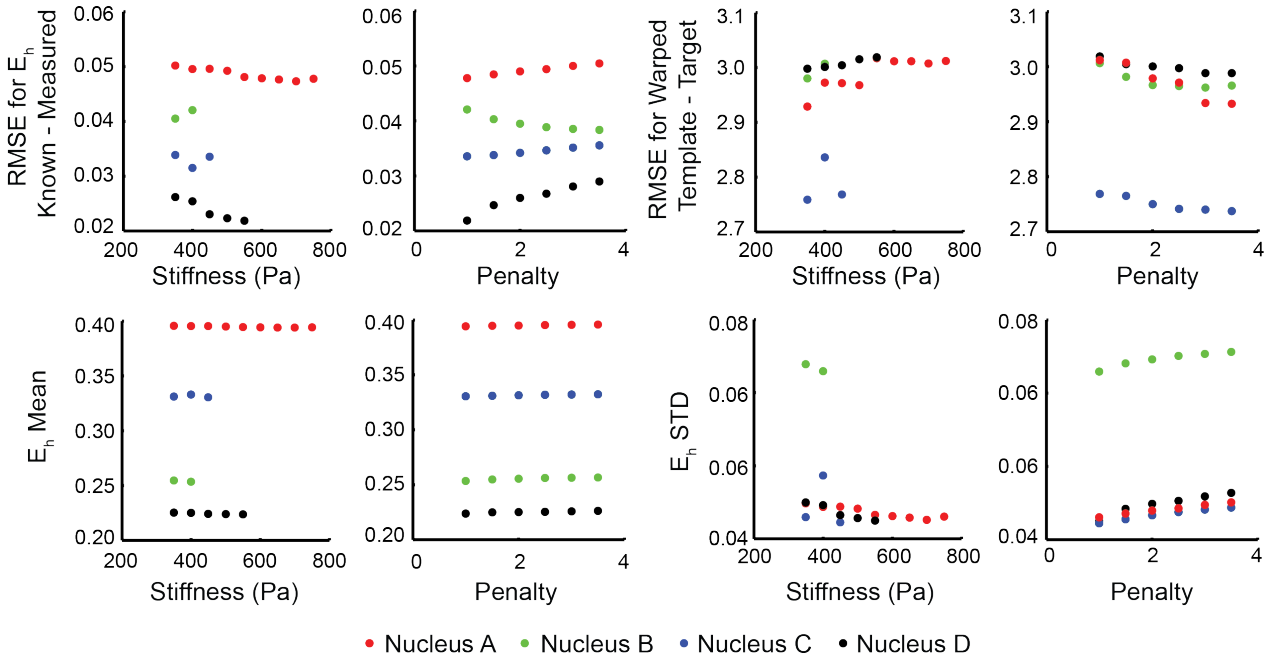

Figure S3. Efficacy of parameter sweep in deformation microscopy, related to Figure 2. To quantify the efficacy of deformation microscopy, the root mean square error (RMSE) was computed comparing the known (forward simulation) and calculated hydrostatic strain. Root mean square error (RMSE) was also computed for image intensity of the warped template and the target. The mean and standard deviation of the hydrostatic strain value was also computed for the nucleus. The results are shown for stiffness and penalty parameter sweep for all four nuclei. The RMSE reaches a minimum with increasing stiffness and penalty, thus reaching the best possible solution. The average of hydrostatic strain is insensitive to both the change in stiffness and penalty. The standard deviation in hydrostatic strain increases with increasing penalty but decreases with increasing stiffness.

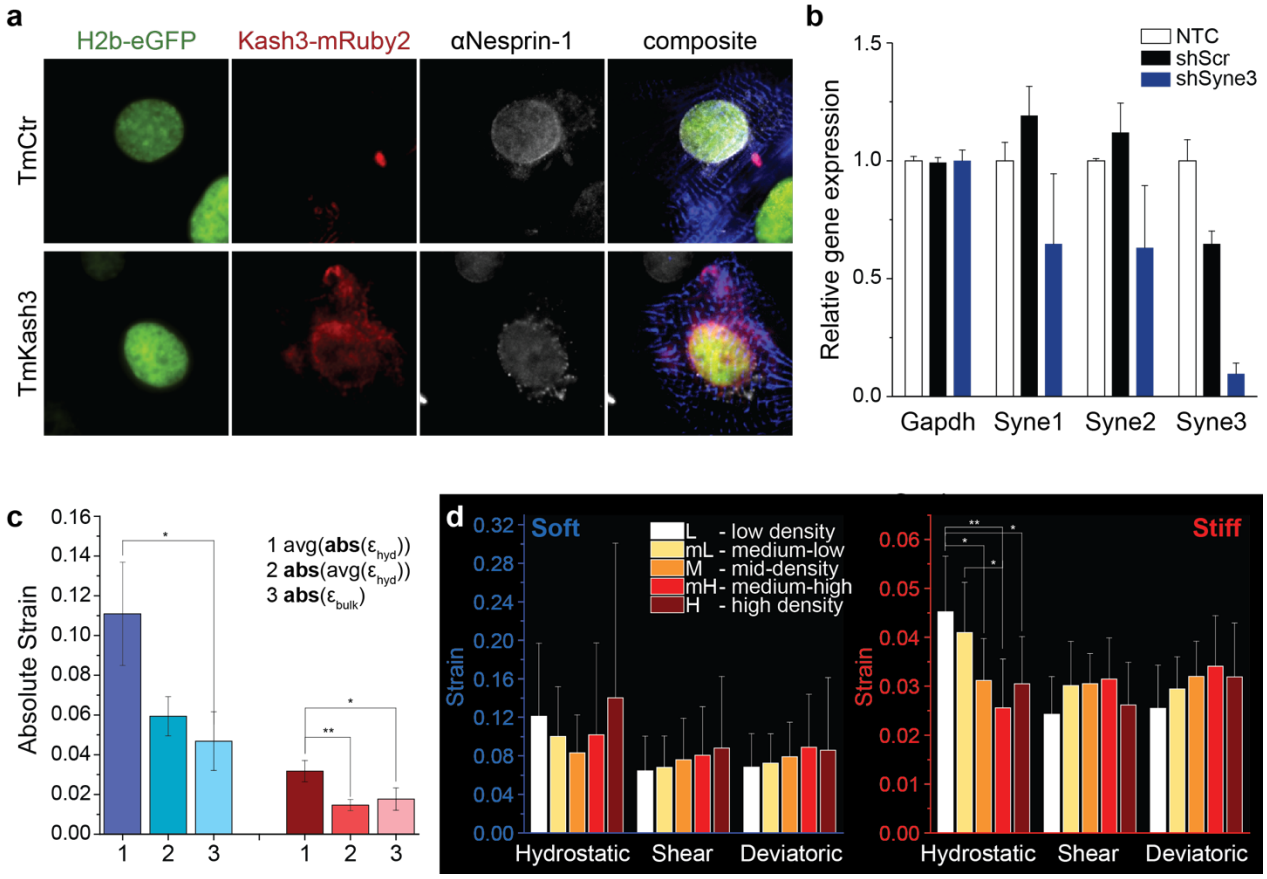

Figure S4. Validation of LINC complex disruption via TmKash3 or shSyne3 in cardiomyocytes, related to Figure 3. (a) Immunofluorescence staining of nesprin-1 in cardiomyocytes transduced with either TmCtr or TmKash3. TmKash3 integrated properly around the nucleus and disrupted the localization of nesprin-1 to the nuclear membrane while TmCtr did not. **(b)** Gene expression analysis of Nesprins (Syne) 1, 2 and 3 between cardiomyocytes transduced with an shRNA cassette against a random scrambled sequence (shScr) or against Syne3 (shSyne3) or non-transduced control cells (NTC); n=4, error=SD. **Comparison of strain obtained using deformation microscopy and bulk strain measurements for cardiomyocyte nuclei, related to Figure 4. (c)** Comparison of deformation microcopy and bulk strain analysis. **(d)** Average strain in each chromatin density segment for nuclei in cardiomyocytes platted on soft or stiff substrates; (b, c): n=5, error=SD, ** $p<0.01$, * $p<0.05$.

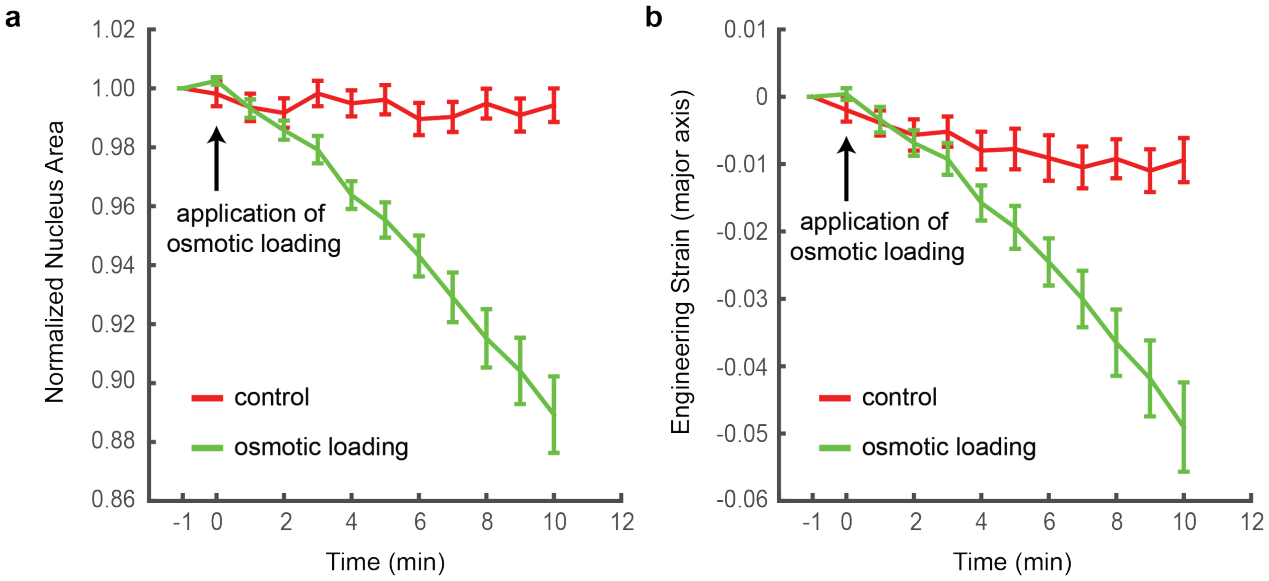

Figure S5. Bulk nuclear strain measurement during hyperosmotic loading of chondrocytes, related to Figure 6. Bulk measurements: **(a)** normalized area and **(b)** engineering strain of P4 chondrocyte nuclei during hyperosmotic loading over time. As water diffuses out of the cell and nucleus, both measures show overall increase in negative compressive strain with time (green). Control cells in medium shows no significant change in those quantities (red); osmotic loading: n=27, control: n=32, error=SD.

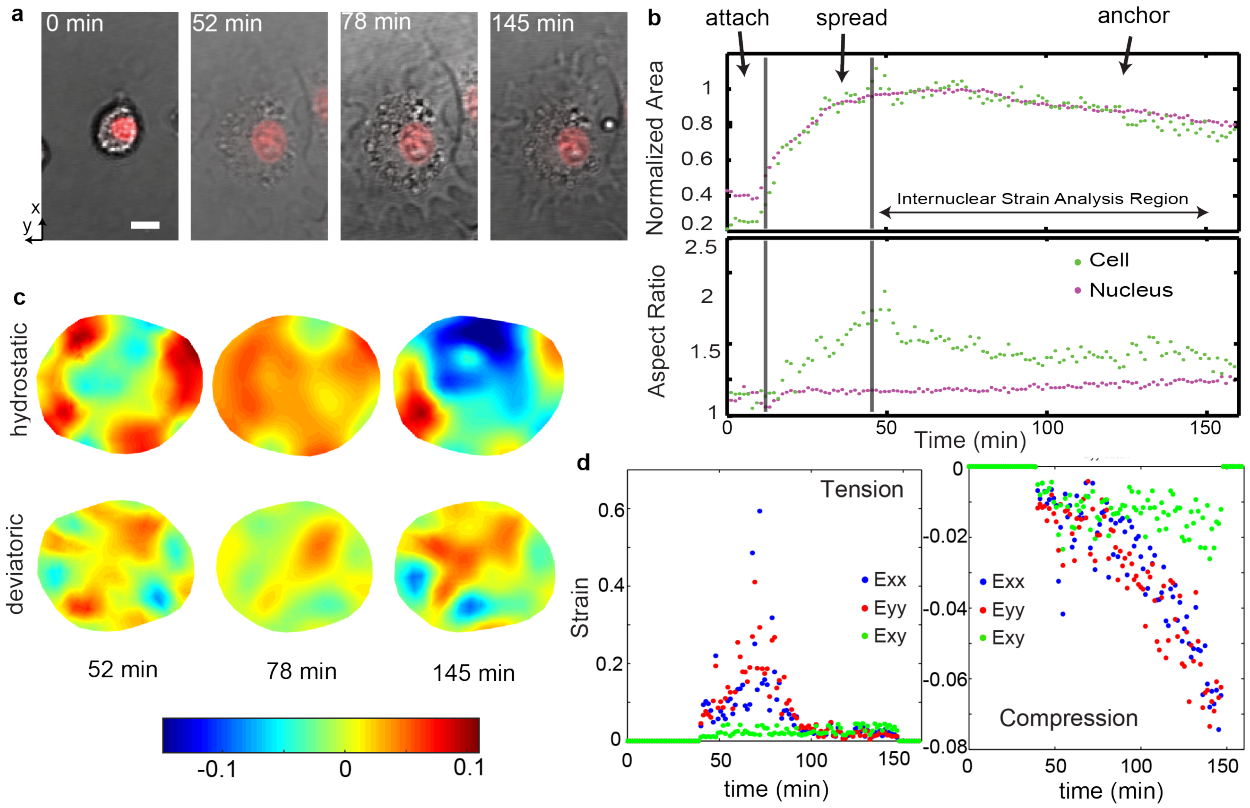

Figure S6. Nuclear deformation during cell spreading, related to discussion, related to STAR METHODS. Deformation microscopy and bulk strain analysis of a P4 chondrocyte nucleus during cell spreading. **(a)** Brightfield microscopy of cell (transmitted) and nucleus (red) during cell spreading. **(b)** Area and aspect ratio change of cell and nucleus indicates different phases during cell spreading. Area and aspect ratio were computed by masking cell and nucleus images in ImageJ. **(c)** Intranuclear strain maps computed via deformation microscopy using the start of the anchoring phase (49 min) as undeformed reference. **(d)** Average tensile and compressive strains over time. Tensile strain showed a temporal spurt from spreading to anchoring phase while compressive strain steadily increased with time.

Table S1. Primer and shRNA hairpin sequences, related to Figure 3. Top: Hairpins with target sequence against nesprin-3 or scrambled control sequence. Hairpin is underlined and bold. Bottom: Primer sequences for qPCR validation of shRNA-mediated nesprin knock-down.

Name	**shRNA Cassette Sequence**	
shSyne 3	CGCTCATGCTTCGGTACAATG**CTCGAG**CATTGTACCGAAGCATGAGCG**TT TTTT**	
shScr	GTGCACACGTTATGGCTACCT**CTCGAG**AGGTAGCCATAACGTGTGCAC**TT TTTT**	
Gene	**Forward Primer**	**Reward Primer**
Gapdh	TGTCAAGCTCATTTCCTGGTATG	GGGATAGGGCCTCTCTTGCT
Syne1	CCAAAGAGCAGGTCCACAAGA	GGTACAAGGCAGGTGAGTCC
Syne2	ACCTTCTTGGAAGAGGAAGAGG	CCCTGATCACCCTTGAGAGGA
Syne3	GACTGCATTCCAGAAGAGTCGG	ACGGCATGCTTTCTGTAGGAG

Methods S1. Deformable image registration and hyperelastic warping, related to STAR Methods

Deformation microscopy uses registration of image data collected in undeformed and deformed states to understand motion internal to objects of interest, e.g., cell nuclei. Consider a space variable X, a displacement map $u(X)$, and a deformation map $\varphi(X)$ defined as

$$\varphi(X) = X + u(X) \tag{1}$$

Deformable image registration methods aim to find the deformation map $\varphi(X)$ which represents minimization of the energy functional, $E(X, \varphi)$, that represents the difference in the strain energy within the deforming material, $W(X, \varphi)$, and an image based energy term, $U(X, \varphi)$, which is a pointwise comparison of the undeformed (template) image T and the deformed (target) image S. This can be mathematically expressed by the following.

$$E(X, \varphi) = \int_{\beta_0} W(X, \varphi) dV - \int_{\beta_0} U\big(T(X, \varphi), S(X, \varphi)\big) dV \tag{2}$$

where the first term on right side is the energy function of the deformation map and the second term is the energy function comprising image comparison. The terms are evaluated at every differential image location dV, and is integrated over the whole image space β_0. For hyperelastic warping, the first term W is the standard energy density function modeled as dependent on the material constitutive model, material properties, and right Cauchy-Green tensor C , defined as $C = F^T F$, where F is the deformation gradient tensor,

$$F(X, \varphi) = \frac{\partial \varphi(X)}{\partial X} \tag{3}$$

The second term U uses a Gaussian tensor model to describe the image energy density functional.

$$U(X, \varphi) = \frac{\lambda}{2}\big(T(X) - S(\varphi)\big)^2 \tag{4}$$

Where T is the scalar intensity field of the template and hence a function of X only. S is the scalar intensity of the target, and hence a function of φ. λ is a penalty parameter that enforces the alignment of the template with the target.

Methods S2. Details of deformation microscopy, related to STAR Methods

Parameter sweep

The goal of deformation microscopy is to reach a pixel intensity matching solution based on the warped template and target images. The iterative hyperelastic warping algorithm is run over a range of two parameters: the material stiffness (range: 100-10000 Pa, with a minimum step size of 100) and the penalty (range: 1-3.5, with a step size of 0.5). For each set of parameters, the root mean square error (RMSE) in intensity difference based on a warped template and target is quantified. The RMSE value was minimized over the parameter sweep and thus the best possible

set of parameters was obtained. A custom-made MATLAB code was written to automate and connect the software for mesh generation (TrueGrid), deformable image registration (nike3D) and postprocessing (WarpLab and LS-PrePost). By using parallel solver for the different penalty parameters, the iterative procedure can be performed in tens of minutes for one nucleus. Figure S1-a explains the iterative procedure and Figure S1-b shows the results of a sequential iterative process to reach the final deformation map.

Sequential spatial filtering

Local minima in the registration process can lead to premature registration for some local image features thus ending up with inaccurate and incomplete registration. To overcome this, sequential low pass filtering is used. First, the larger image features, e.g. object boundaries and coarse texture details, are registered (global registration) followed by registration of finer details (local registration) by gradually reducing the extent of the spatial filter. The spatial filter is applied by convolution of the image with a kernel $\kappa(X)$. For the image field T,

$$T * (X) = \varphi(X) * \kappa(X) = \int_B T(X)\kappa(X - Z)dZ \qquad (5)$$

where Z is the frequency domain variable of X and $T * (X)$ is the spatial intensity data in the filtered image in the iteratively deformed domain B. In this particular study, a 3D Gaussian kernel has been used.

$$\kappa(X) = A\ exp\left(-\frac{X \cdot X}{2\sigma^2}\right) \qquad (6)$$

Where σ^2 is the spatial variance used to control the extent of blurring and A is a normalizing constant.

Underregistration and overregistration

During the deformable registration process, the deformed template may be underregistered at certain parameter values, despite the blurring applied to that that particular parameter. This leads to a false minimum total energy E and the deformation values we obtain are not optimal. On the other hand, if in equation 2, the U term is larger than the W term, the minimized energy becomes negative in some spaces and a false deformation is reported termed as 'overregistration'. This is demonstrated in Figure S1-b, for the two parameters stiffness and penalty.

Methods S3. Validation of deformation microscopy, related to STAR Methods

Validation of deformation microscopy was determined using known forward simulations of deformation under loading. The accuracy and reliability of the technique was validated for all image types, but we specifically demonstrate the validation for nucleus images.

Images of passage four chondrocytes (P4, exhibiting a fibroblast-like phenotype) were captured by fluorescence confocal microscopy (Nikon A1R) with DNA staining (DRAQ5; Cell Signaling), at 0.5 μM concentration. More compact heterochromatin regions were stained brighter compared to euchromatin regions. The euchromatin and heterochromatin regions were

segmented using a custom algorithm based on the computation of the second derivative of image intensity values.

To account for unknown material properties of nuclear subregions, we assigned different stiffness values to heterochromatin and euchromatin areas defined by segmentation of confocal images (Figure 2-a). Four different cases were used, representing maximum and minimum stiffness expected in the heterochromatin and euchromatin subregions: nucleus A (H:E=1:10), nucleus B (H:E=10:1), nucleus C (H:E=2:1) and nucleus D (H:E=1:2). A linear elastic material model was used for the validation and the warping analysis. The nucleus deformation was simulated in ANSYS by applying equal tensile normal force on the nuclear periphery as the boundary condition, so that the magnitude of deformation was similar to that observed in our previous studies (Henderson *et al.*, 2013). The difference between known (simulated) and computed strain measures at same spatial coordinates were used to validate the deformation microscopy technique with a difference of 0 representing perfect registration. The coefficient of determination was calculated between simulated and computed strain to further measure the efficacy of hyperelastic warping microscopy.

As shown in Figure 2-b, deformation microscopy was capable of reliable strain and chromatin organization quantification over an order of magnitude range of material property values. Euchromatin (E) is thought to have lower stiffness than heterochromatin (H), and hence the comparatively less accurate registration was observed for a low material property ratio (i.e. H:E = 1:10) case where some elements near the nuclear periphery had overestimated strain values. This was further quantitatively validated by comparing known deformation with computed deformation (Figure 2-c), where Nucleus B (H:E = 10:1) yielded the most accurate measurement followed by Nucleus C (H:E = 2:1). While this technique provided detailed intranuclear deformation maps, bulk mechanical measurements alone result in unreliable strain quantification (Figure S2-a). Further, the deformation in the intranuclear space was found be related to the local chromatin density, and hence to the image intensity (Figure S2-b,c,d). The sensitivity of the deformation measurement with regard to the key parameters (material stiffness and penalty factor) was also analyzed (Figure S3), and we found that, based on the specific application, an optimal combination of those two parameters lead to the best registration results.

Methods S4. Strain measures to quantify deformation, Related to STAR methods

Deformable microscopy directly yields displacement measures, which leads to fundamental strain measures. For our two-dimensional (2D) analysis, as performed in this work using the z projection of the images, the relevant strain measures computed are: E_{xx}, E_{yy} and E_{xy}.
The hydrostatic strain can be derived from those quantities as:

$$E_{hyd} = \frac{E_{xx} + E_{yy}}{2}$$

The first and second deviatoric strains are computed as:

$$E_{d1} = E_{xx} - E_{hyd} = \frac{E_{xx} - E_{yy}}{2}$$

$$E_{d2} = E_{hyd} - E_{yy} = \frac{E_{yy} - E_{xx}}{2}$$

Therefore, $E_{d1} = -E_{d2}$ for 2D measurement. Unless otherwise mentioned all quantifications of deviatoric strain in this study are the second deviatoric strain. Note that this relation does not hold true for three-dimensional (3D) measurements. For this work, all nucleus deformation experiments are performed on cells plated on 2D surface, therefore the z directional strain has a minimum effect on the two-dimensional strain measurement. However, these methods can be applied and extended to 3D strain measurement (Henderson *et al.*, 2013).